Chanoclavine synthase operates by an NADPH-independent superoxide mechanism

Chen, Chun Chi; Yu, Zhi Pu; Liu, Ziwei; Hagedoorn, Peter Leon; Schmitz, Rob Alexander; Liu, Aokun; Huang, Jian Wen; Guo, Rey Ting; Gao, Shu Shan; More Authors

DOI
10.1038/s41586-025-08670-3

Publication date
2025

Document Version
Final published version

Published in
Nature

Article

Chanoclavine synthase operates by an NADPH-independent superoxide mechanism

https://doi.org/10.1038/s41586-025-08670-3

Received: 23 August 2024

Accepted: 17 January 2025

Published online: 5 March 2025

Open access

Check for updates

Chun-Chi Chen[1,2,3,10], Zhi-Pu Yu[2,4,10], Ziwei Liu[1,3,10], Yongpeng Yao[5,10], Peter-Leon Hagedoorn[6], Rob Alexander Schmitz[6], Lujia Yang[2,7], Lu Yu[8], Aokun Liu[8,9], Xiang Sheng[2,7], Hao Su[2,7], Yaqing Ma[2], Te Wang[3], Jian-Wen Huang[1,3], Lilan Zhang[3], Juzhang Yan[2,7], Jinping Bao[2,7], Chengsen Cui[2,7], Xian Li[1,3], Panpan Shen[1,3], Wuyuan Zhang[2,4], Jian Min[3], Chang-Yun Wang[4], Rey-Ting Guo[1,3]✉ & Shu-Shan Gao[2,7]✉

More than ten ergot alkaloids comprising both natural and semi-synthetic products are used to treat various diseases[1,2]. The central C ring forms the core pharmacophore for ergot alkaloids, giving them structural similarity to neurotransmitters, thus enabling their modulation of neurotransmitter receptors[3]. The haem catalase chanoclavine synthase (EasC) catalyses the construction of this ring through complex radical oxidative cyclization[4]. Unlike canonical catalases, which catalyse H_2O_2 disproportionation[5,6], EasC and its homologues represent a broader class of catalases that catalyse O_2-dependent radical reactions[4,7]. We have elucidated the structure of EasC by cryo-electron microscopy, revealing a nicotinamide adenine dinucleotide phosphate (reduced) (NADPH)-binding pocket and a haem pocket common to all haem catalases, with a unique homodimeric architecture that is, to our knowledge, previously unobserved. The substrate prechanoclavine unprecedentedly binds in the NADPH-binding pocket, instead of the previously suspected haem-binding pocket, and two pockets were connected by a slender tunnel. Contrary to the established mechanisms, EasC uses superoxide rather than the more generally used transient haem iron–oxygen complexes (such as compounds I, II and III)[8,9], to mediate substrate transformation through superoxide-mediated cooperative catalysis of the two distant pockets. We propose that this reactive oxygen species mechanism could be widespread in metalloenzyme-catalysed reactions.

Ergot alkaloids (Supplementary Fig. 1a) are widely used to treat various diseases, and in 2024, lysergic acid diethylamide (Supplementary Fig. 1b), a semi-synthetic ergot alkaloid, received breakthrough therapy designation from the Food and Drug Administration for generalized anxiety disorder, affecting 2.7% of the US population (https://www.nimh.nih.gov/health/statistics/generalized-anxiety-disorder). Ergot alkaloids comprise more than 70 natural products from fungi and plants[10,11], as well as numerous semi-synthetic ones[1] (Supplementary Fig. 1). These alkaloids act as agonists or antagonists at various adrenergic, serotonergic and dopaminergic receptors[2,11], influencing physiological systems, such as the vascular smooth muscle, central nervous system and endocrine system[2]. This broad action underlies their use in treating conditions, such as acute migraines, postpartum haemorrhage, hyperprolactinaemia, Parkinson's disease and Alzheimer's disease[1,2] (Supplementary Fig. 1a).

The structural similarity of an ergot-alkaloid pharmacophore (ergoline) with biogenic amine receptors (dopamine, serotonin and noradrenaline) enables receptor modulation[3] (Fig. 1 and Supplementary Fig. 1). The critical step in tetracyclic ergoline biosynthesis is the assembly of the central C ring (Fig. 1 and Supplementary Fig. 1c), catalysed by the haem catalase chanoclavine synthase (EasC)[4] through O_2-dependent oxidative cyclization. CnsD, a homologue of EasC, was recently identified to perform O_2-dependent radical decarboxylation in the biosynthesis of anti-tumour communesins[7]. Hence, with catalases regarded as the oldest and most common enzymes in aerobic cells and H_2O_2 disproportionation identified as their sole function so far[5,6] (Supplementary Fig. 2a), EasC and its homologues emerge as a distinct division of catalases that use O_2 to catalyse radical reactions[4,7]. Phylogenetic analysis also demonstrated that they belong to a separate clade that differs from all known ones[4].

[1]Zhejiang Key Laboratory of Medical Epigenetics, Department of Immunology and Pathogen Biology, School of Basic Medical Sciences, Hangzhou Normal University, Hangzhou, People's Republic of China. [2]State Key Laboratory of Engineering Biology for Low-Carbon Manufacturing, Tianjin Institute of Industrial Biotechnology, Chinese Academy of Sciences, Tianjin, People's Republic of China. [3]State Key Laboratory of Biocatalysis and Enzyme Engineering, Hubei Hongshan Laboratory, School of Life Sciences, Hubei University, Wuhan, People's Republic of China. [4]MOE Key Laboratory of Marine Drugs and Key Laboratory of Evolution and Marine Biodiversity, School of Medicine and Pharmacy, Institute of Evolution & Marine Biodiversity, Ocean University of China, Laboratory for Marine Drugs and Bioproducts, Qingdao Marine Science and Technology Center, Qingdao, People's Republic of China. [5]State Key Laboratory of Mycology, Institute of Microbiology, Chinese Academy of Sciences, Beijing, People's Republic of China. [6]Biocatalysis, Department of Biotechnology, Delft University of Technology, Delft, The Netherlands. [7]National Center of Technology Innovation for Synthetic Biology, Tianjin, People's Republic of China. [8]Division of Life Sciences and Medicine, University of Science and Technology of China, Hefei, People's Republic of China. [9]High Magnetic Field Laboratory, Hefei Institutes of Physical Science, Chinese Academy of Sciences, Hefei, People's Republic of China. [10]These authors contributed equally: Chun-Chi Chen, Zhi-Pu Yu, Ziwei Liu, Yongpeng Yao. ✉e-mail: guoreyting@hznu.edu.cn; gaoss@tib.cas.cn

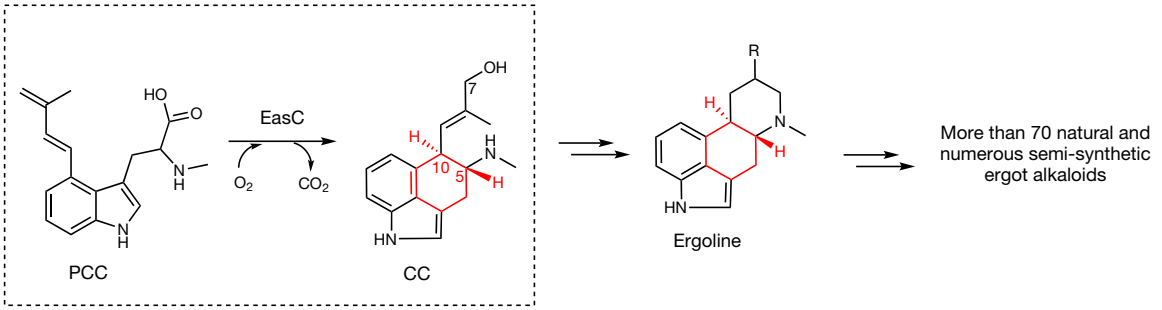

Fig. 1 | EasC in the biosynthesis of medicinal ergot alkaloids. The tetracyclic ergoline with a central C ring (marked in red) is the pharmacophore for all clinically applied ergot alkaloids.

Central C ring construction requires regio- and stereoselective formation of the C_5–C_{10} bond between sp^2 and sp^3 hybridized carbons (Fig. 1). Instead of direct C–H activation, EasC catalyses oxidative cyclization, which involves decarboxylation, C_5–C_{10} bond formation and hydroxylation at the terminal alkene (Fig. 1). The proposed mechanism for EasC (Supplementary Fig. 2b), similar to P450s, involves the compound I (Cpd I) initiated oxidative cyclization through hydrogen abstraction at the carboxylate group of prechanoclavine (PCC)[4,7,12]. After radical rearrangement for decarboxylation, C_5–C_{10} bond formation and hydroxyl rebound from compound II (Cpd II), the transformation is completed, producing chanoclavine (CC) (Supplementary Fig. 2b). However, inherent structural differences, such as the nature of the axial ligand, complicate the direct application of the P450 catalytic mechanism in catalases[8]. Thorough elucidation of the catalytic mechanism of EasC using structural biology and spectroscopy is crucial because existing catalase studies focused on H_2O_2 disproportionation and have limitations in fully understanding the O_2-dependent radical reactions.

In metalloenzyme-catalysed O_2-dependent reactions, a metal–oxygen complex mediates substrate transformation because the direct reaction of O_2 with an organic substrate is spin-forbidden and energetically unfavourable[9]. In haem enzymes[8], the process is divided into two parts: O_2 activation and substrate transformation. The enzyme reduces O_2 by means of the haem iron, forming iron–oxygen complexes (Cpd I, II, III and so on), which then transform the substrate. This 'metal–oxygen' mode, established for decades, involves substrate binding above the haem and the occurrence of O_2 activation and substrate transformation in the same pocket. In this study, we identified a superoxide mechanism distinct from this metal–oxygen mode in the metalloenzyme chemistry.

EasC is a homodimer

The structure of EasC from *Claviceps fusiformis* ($EasC_{Cf}$) was resolved using single-particle cryo-electron microscopy (cryo-EM) at a resolution of 2.64 Å (Extended Data Fig. 1a, Supplementary Fig. 3 and Supplementary Table 2). $EasC_{Cf}$ exhibits a canonical catalase fold, featuring a conserved haem-binding pocket deeply embedded within the protein, a nicotinamide adenine dinucleotide phosphate (reduced) (NADPH)-binding pocket and a hydrophobic core formed by an eight-stranded antiparallel β-barrel (β1–8)[13] (Extended Data Fig. 1b). Unlike typical tetrameric catalases (Extended Data Fig. 1d), $EasC_{Cf}$ exists as a homodimer (Extended Data Fig. 1a), and the size-excluded chromatography analyses also indicate that $EasC_{Cf}$ exists in solution only as a dimer (Extended Data Fig. 1c).

The three-dimensional haem environment is shown in Extended Data Fig. 2a, which is constructed using amino acids as in other catalases[14], with residues H53 and F139 associated with the distal side and Y343 and R339 associated with the proximal side of the haem. Similar to known typical catalases[14], a tyrosine residue (Y343) occupies the fifth coordination site, with the phenolate oxygen 2.0 Å from the haem iron (Extended Data Fig. 2a). A channel linking the opening to haem measures approximately 15 Å in length and 1.42 Å at its narrowest point (Extended Data Fig. 2b,c). The channel entrance is lined with residues L177, Q146 and D106, whereas hydrophobic residues T94, V143, F132, F131 and L142 form the channel itself (Extended Data Fig. 2c). Given the bulky size of substrate PCC (7.0 × 8.5 Å), the slender opening channel is unlikely to permit its entry into the haem pocket (Extended Data Fig. 2c).

PCC binds in the NADPH-binding pocket

The $EasC_{Cf}$ complex was further solved using single-particle cryo-EM at a resolution of 2.33 Å in the presence of PCC (Supplementary Fig. 4 and Supplementary Table 2). The electron density was clear for residues 33–351 and 378–471. Unexpectedly, no extra electron density was observed above the haem, and both NADPH-binding pockets in the homodimer contained the electron density that can be confidently modelled with PCC (Fig. 2a,b). The binding of the substrate in the NADPH-binding pocket aligned with the structural feature of the slender opening channel (Extended Data Fig. 2c).

Superimposition of the apo-form and PCC-bound $EasC_{Cf}$ revealed a Cα root mean square deviation of only 0.4 Å, which indicates that PCC binding exerts minimal impact on the overall protein conformation (Extended Data Fig. 3a). Notably, a fragment (N221–N234) absent in the apo form was present in the PCC complex (Extended Data Fig. 3b,c), forming the β6–α5 loop that extends to cap the PCC-binding site. Residue F222 within this loop interacts with the indole ring of PCC through T-stacking (Extended Data Fig. 3d), which indicates that substrate binding may stabilize the β6–α5 loop in $EasC_{Cf}$.

PCC bound perpendicularly to haem, with a 20.6-Å closest approach from the carbonyl-C atom to the haem centre (Fig. 2c). The indole moiety and C4 alkyl group interacted with the hydrophobic surface formed by Y286, M130, F181 and F185, whereas the carboxylate group formed a hydrogen bond with Y193 (Fig. 2b and Extended Data Fig. 4a). The alanine substituents of these residues showed very low enzyme activity (Extended Data Fig. 4b), as isothermal titration calorimetry (ITC) studies confirmed significantly decreased substrate binding affinity in F185A and Y193A mutants compared to the wild-type enzyme (Extended Data Fig. 4c).

Our attempts to obtain the NADPH-bound complex of $EasC_{Cf}$ were unsuccessful. $EasC_{Cf}$ has two extended loops (β7–β8 and β6–α5) that protrude into the NADPH-binding pocket, conflicting with NADPH binding according to molecular docking (Extended Data Fig. 1f). Additionally, key polar residues in human erythrocyte catalase that interacted with NADPH (R203, K237 and H305) were replaced by hydrophobic residues (F181, A215 and L283) in $EasC_{Cf}$ (Extended Data Fig. 1g and Supplementary Fig. 5). Thus, $EasC_{Cf}$ is unlikely to bind to or depend on NADPH.

A tunnel connects the haem- and NADPH-binding pockets

Using CAVER v.3.0.3, we identified a slender 11.6-Å tunnel linking the haem and NADPH-binding pockets (Fig. 2d), composed mainly of

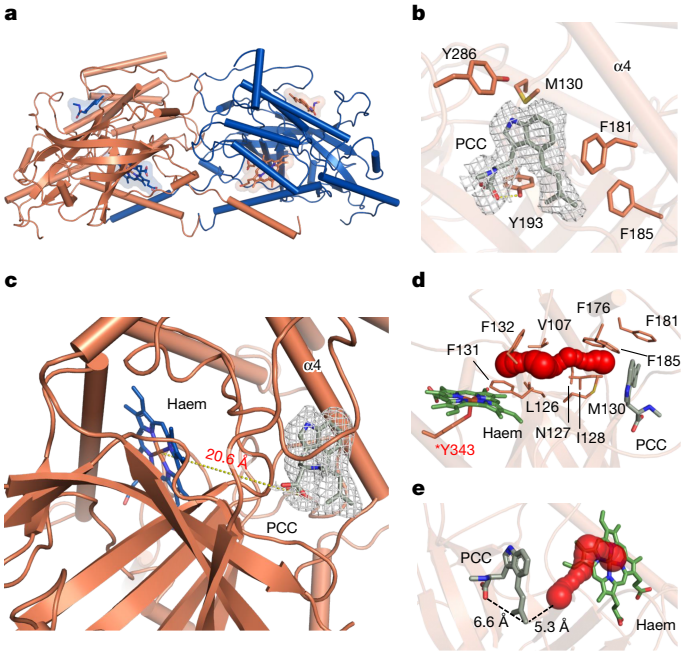

Fig. 2 | Complex structure of $EasC_{Cf}$ and PCC. a, Overall structure of the complex of $EasC_{Cf}$ with PCC. **b**, The NADPH-binding pocket of $EasC_{Cf}$–PCC complex. **c**, The relative positions of haem and PCC in $EasC_{Cf}$–PCC complex. **d**, Key amino residues forming the tunnel that connects the haem pocket and NADPH-binding pocket. The channel length was about 11.6 Å, and the central channel residues are marked in orange. Residue Y343 that served as the fifth coordinated ligand of the haem iron is noted by an asterisk. **e**, The structure of the tunnel observed from the substrate's perspective, indicating that $EasC_{Cf}$ binds PCC with its C4 alkyl group orienting towards the opening of the tunnel. α4 indicates the fourth α-helix. In **b**,**c**, the density map of PCC is shown in mesh at 3.0σ contour level.

hydrophobic amino acids (F185, F176, F132, V107, L126, N127, I128 and M130). The C4 alkyl group of PCC aligned with the tunnel opening at a distance of 5.3 Å (Fig. 2e). Mutating some residues to smaller alanine slightly increased the catalytic activity of $EasC_{Cf}$, whereas increasing the size of their side chain by mutating to Phe severely affected the enzyme activity (Supplementary Fig. 6). This indicates the presence of a tunnel, which may facilitate the transfer of certain reactive oxygen species (ROS) to react with the 1,3-diene of the C4 alkyl group or its radicals. A similar tunnel in flavin-dependent halogenase PrnA guides ROS HOCl for regioselective chlorination[15].

NADPH does not act as an electron donor

EasC was previously thought to be NADPH dependent because EasC from *Aspergillus fumigatus* ($EasC_{Af}$) converts only minor PCC in a 2-h reaction without NADPH[4]. Characterizing PCC binding in the NADPH pocket promoted a reevaluation of the role of NADPH. ITC tests indicate that $EasC_{Cf}$ does not bind to NADPH (Supplementary Fig. 7). Revisiting the 2-h reactions of $EasC_{Af}$ and $EasC_{Cf}$ indicates that both enzymes fully converted PCC in the presence of NADPH. By contrast, they achieved only approximately 15 and 50% conversion without NADPH, respectively (Extended Data Fig. 5a). Extending the reaction time to 24 h resulted in full conversion under all conditions (Extended Data Fig. 5a).

We systematically tested the influence of nicotinamide adenine dinucleotide (reduced form) (NADH), nicotinamide adenine dinucleotide (oxidized form) (NAD^+), nicotinamide adenine dinucleotide phosphate (oxidized form) ($NADP^+$) and small-molecule reducing agents (sodium ascorbate and glutathione) on EasC activity. Except for sodium ascorbate, all tested molecules could accelerate the reactions of $EasC_{Af}$ and $EasC_{Cf}$ (Extended Data Fig. 5b,c). These findings indicate that NADPH may accelerate the EasC reaction either by stabilizing the protein (catalase is known to generate radical species[16] that disrupt protein stability) or through protein–molecule interaction. Indeed, $EasC_{Cf}$ isolated from the reaction mixture without NADPH exhibited a different circular dichroism spectrum (Extended Data Fig. 5d), showing a noticeable decrease in the negative ellipticity amplitude at approximately 205 nm and a slight ultraviolet shift of approximately 2 nm, indicating potential conformational changes in certain α-helices or β-sheets. These differences became more pronounced with extended reaction time (Extended Data Fig. 5d).

Identification of the compound III intermediate

The unexpected finding on the binding of PCC in the NADPH-binding pocket raised a question about whether the haem pocket still participates in O_2 activation. To investigate this, we mutated six $EasC_{Cf}$ residues (R50, R90, F319, R339, Y343 and L39) that are involved in the binding of haem (Extended Data Fig. 6a). The mutants exhibited a colour change from brown to colourless, with comparable protein expression levels (26–28 mg l^{-1}; Extended Data Fig. 6b), and all showed significant reductions in PCC conversion (Extended Data Fig. 6c). Circular dichroism spectra indicate that the conformations of these mutants were nearly identical to those of the wild type, except in the case of F319A and R339A (Extended Data Fig. 6d), suggesting that the loss of activity in mutants L39, R50, R90 and Y343 is due to the loss of haem, and not a change in protein structure.

To further probe the role of the haem pocket, we used the known catalase inhibitors NaN_3 and NH_2OH, which are ligands to the haem Fe centre[17]. Both inhibitors reduced $EasC_{Cf}$ activity in a concentration-dependent fashion with a constant reflecting 50% inhibition (IC_{50}) of 2.90 and 0.72 mM (Extended Data Fig. 6e), respectively. Moreover, the $EasC_{Cf}$ activity could be restored while NaN_3 was filtered out from the reaction mixture (Extended Data Fig. 6f), confirming that the inhibition of the $EasC_{Cf}$ reaction results from its interaction with haem.

To characterize the active iron–oxygen complex (Cpd I, Cpd II or compound III (Cpd III)) involved in the EasC reaction, we used stopped-flow spectroscopy. Upon rapid mixing of a solution of ferric $EasC_{Cf}$ with PCC under aerobic conditions, a new intermediate with absorption maxima at 416, 544 and 590 nm was observed (Fig. 3a and Extended Data Fig. 7a), in which the α/β region becoming more pronounced from 540 to 600 nm. The spectral features are markedly different from the reported spectroscopic characteristics of Cpd I with absorption maxima at approximately 408 and 650 nm (refs. 18,19), consistent with Cpd III complexes observed in known haem enzymes[18–20], and the $EasC_{Cf}$ Cpd III generated by mixing ferrous $EasC_{Cf}$ with air-saturated buffer[18] (Supplementary Fig. 8), suggesting that the EasC reaction follows a Cpd III centred pathway instead of the previously proposed Cpd I centred pathway.

Reduction conditions for Cpd III generation

Two catalytic cycles involving electron transfer from a donor to the ground state of the ferric enzyme Fe(III) have been established for Cpd III (Fe(II)-O_2 or Fe(III)-O_2^-) formation in haem enzymes. One cycle necessitates the formation of the ferrous enzyme Fe(II) for O_2 binding and Cpd III formation[21,22], whereas the other couples electron transfer and O_2 binding directly, bypassing the ferrous intermediate[23].

Because NADPH has been ruled out as the electron donor in the EasC system, PCC has emerged as the sole source. To probe the reduction potential of ferric EasC, electron paramagnetic resonance (EPR) spectroscopy was conducted under various conditions (Fig. 3b and Supplementary Figs. 9–11). The EPR spectrum of anaerobically pretreated $EasC_{Cf}$ under anaerobic conditions showed a characteristic

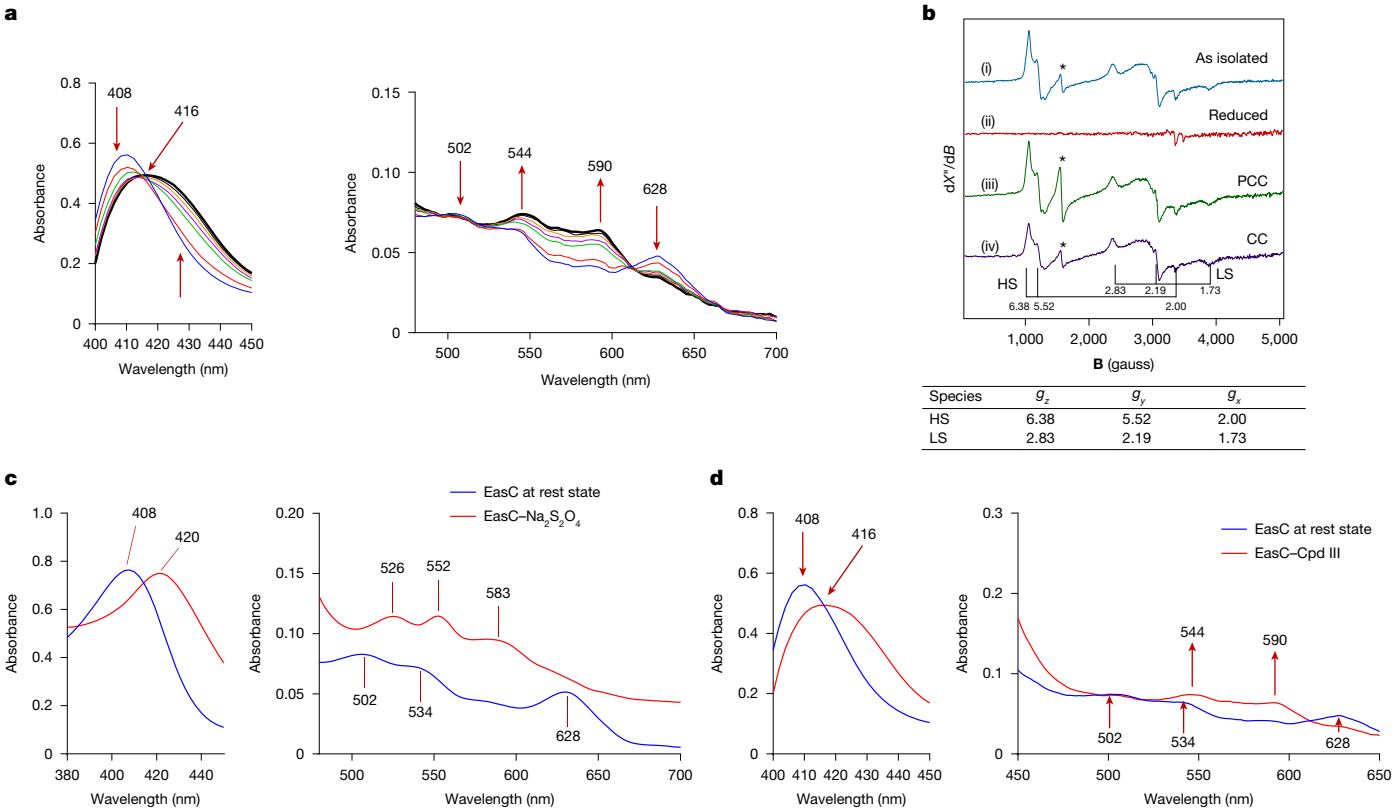

Species	g_z	g_y	g_x
HS	6.38	5.52	2.00
LS	2.83	2.19	1.73

Fig. 3 | Probing the reduction conditions of ferric EasC for Cpd III generation. **a**, Stopped-flow UV–Vis spectra obtained on reaction of ferric 40 µM $EasC_{Cf}$ with 0.5 mM PCC, monitored over 1 s, showing formation of Cpd III (black line; λ_{max} = 416, 544 and 590 nm). **b**, EPR spectroscopy of $EasC_{Cf}$. (i) 492 µM $EasC_{Cf}$, (ii) 442 µM $EasC_{Cf}$ with 10 mM sodium dithionite, (iii) 480 µM $EasC_{Cf}$ and 5.19 mM PCC and (iv) 480 µM $EasC_{Cf}$ and 4.93 mM CC. All the spectra were recorded under anaerobic conditions. The asterisk indicates the g = 4.3 signal characteristic of non-specifically bound mononuclear Fe(III). **c**, UV–Vis absorptions of ferric $EasC_{Cf}$ at rest state and ferrous $EasC_{Cf}$ reacted with 2 mM sodium dithionite. **d**, Stopped-flow UV–Vis spectra of ferric $EasC_{Cf}$ at rest state and $EasC_{Cf}$ Cpd III. EasC noted in the figure is $EasC_{Cf}$. HS, high spin; LS, low spin.

mixture of high-spin species typical of ferric catalases[24,25], along with low-spin signals that may present adducts arising from the sample preparation (most probably residual imidazole from Ni–NTA purification). After reduction with sodium dithionite, these signals completely disappeared (Fig. 3b), confirming that (1) resting state $EasC_{Cf}$ is clearly ferric and (2) the haem iron can be completely reduced with excess sodium dithionite. The midpoint reduction potential for $EasC_{Cf}$ was determined to be −103 ± 5 mV (Supplementary Fig. 12) using Massey's xanthine oxidase reduction assay[23] (see Supplementary Method for details), which is close to the reported reduction potential of the oxygen/superoxide redox couple[26]. Further addition of PCC or CC to either ferric or ferrous EasC under anaerobic conditions did not change the haem signals (Fig. 3b and Supplementary Fig. 11), consistent with the absence of direct coordination to haem by the substrate and product and the inability of PCC to reduce ferric Fe under anaerobic conditions.

Aligned with the EPR findings, the ultraviolet–visible (UV–Vis) absorption of $EasC_{Cf}$ under anaerobic conditions displayed the classic features of a five-coordinate high-spin ferric Fe(III) haem (EasC resting state), with absorption maxima at 408, 502, 534 and 628 nm (ref. 27) (Fig. 3c and Extended Data Fig. 7b). When sodium dithionite was added under anaerobic conditions, the UV–Vis absorption of ferrous $EasC_{Cf}$ (reduced form) exhibited a redshift of the Soret band from 408 to 420 nm, with absorption maxima at 526, 552 and 583 nm (Fig. 3c and Extended Data Fig. 7b). However, no such shift occurred upon the addition of NADPH and PCC (Extended Data Fig. 7c), further confirming that NADPH is not the electron donor and that PCC cannot reduce ferric EasC under anaerobic conditions.

Finally, we re-examined the stopped-flow data of $EasC_{Cf}$ with PCC under aerobic conditions focusing on two specific time points (1 and 751 ms; Fig. 3d). The spectra feature ferric Fe(III) ion (EasC resting state) and Cpd III, respectively. These absorption shifts indicate the transformation of Fe(III) to Cpd III, where Fe(III) gains an electron from PCC concomitant with O_2 binding to form Cpd III. Thus, PCC can reduce ferric $EasC_{Cf}$ under aerobic conditions.

Electron transfer mechanism to generate Cpd III

The binding of PCC in the NADPH-binding pocket raised the question of how long-range electron transfer from PCC to haem is achieved. As such, electron transfer under anaerobic conditions has been ruled out; therefore, we proposed that a concerted mechanism, which directly leads to Fe(III)-O_2^- species in the presence of O_2, bypasses the formation of the generally assumed Fe(II) species (Fig. 5 and Extended Data Fig. 8). Enhancing of the electron transfer in the presence of O_2 has been documented in lytic polysaccharide monooxygenases[28], ascorbate oxidase[29], cytochrome c oxidase[30] and peroxidase KatG[23]. Compared with electron transfer in the absence of O_2, the presence of O_2 increases the electron transfer rate, primarily because of the extra driving force arising from exothermic O_2 binding[31]. For instance, in the KatG system, electron transfer from the Met-Tyr-Trp adduct to Fe(III) occurs only upon O_2 binding[25]. Additionally, amino acids, including cysteine, histidine, methionine, phenylalanine, tryptophan and tyrosine, are known to act as relay amino acids for long-distance electron transfer[32,33].

We identified a group of spatially adjacent amino acids (M130, F131 and F132) as potential relay amino acids positioned 3.7 and 4.4 Å from

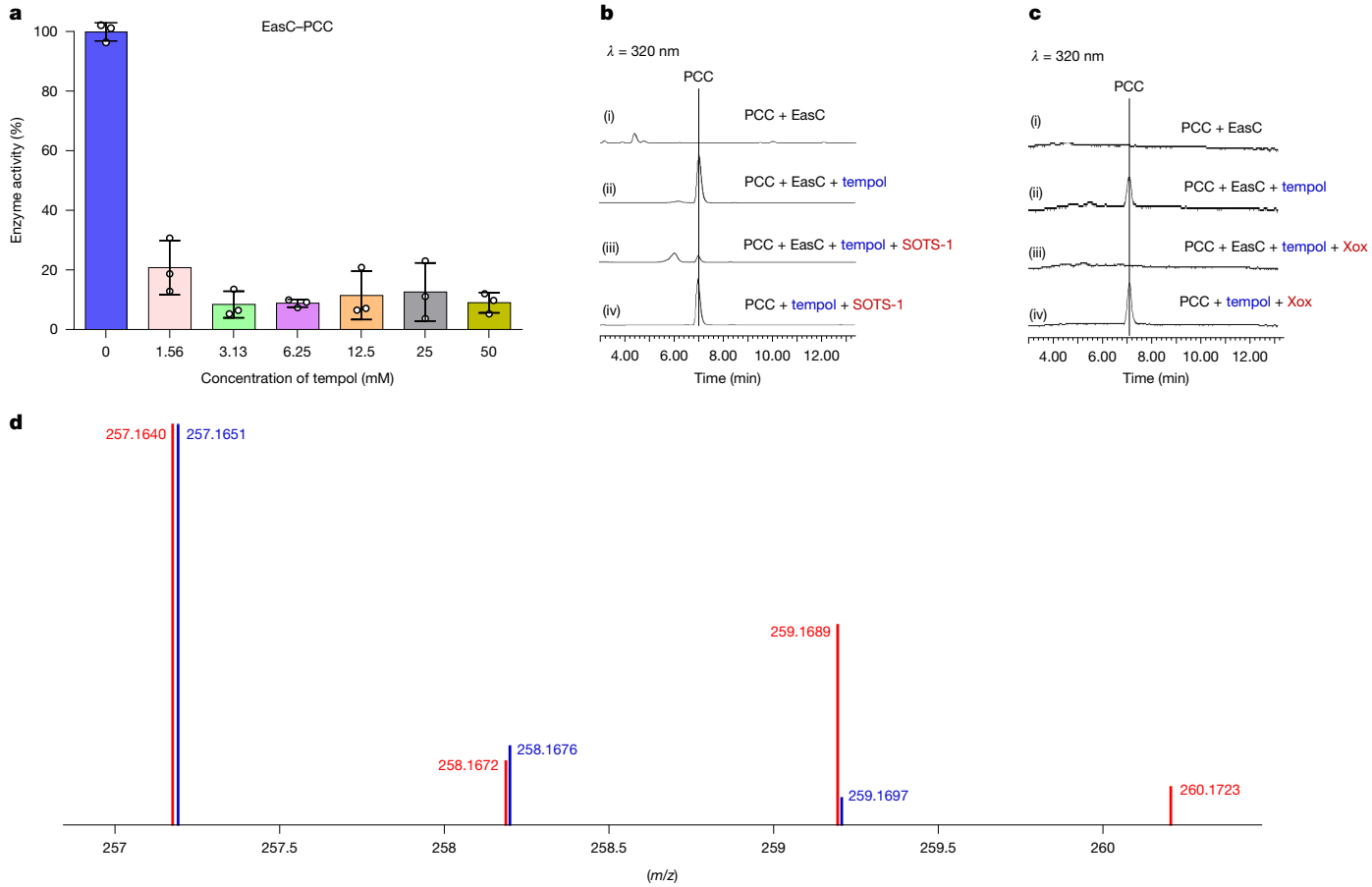

Fig. 4 | Superoxide from Cpd III mediates the cooperative catalysis of two distant pockets. a, Detailed inhibitory data of superoxide scavenger tempol towards $EasC_{Cf}$ activity. The reaction system generally consisted of 20 μM enzyme, 0.5 mM PCC and 2 mM NADPH. A triplicate assay was conducted. The enzyme activity of each sample was calculated as a percentage of the control sample. The individual ($n = 3$) and average values along with error bars (s.d.) of each group in one representative experiment among three independent experiments are shown. **b**, High-performance liquid chromatography (HPLC) profiles of the restoration of SOTS-1 of the tempol-inhibited $EasC_{Cf}$ activity. HPLC profiles were recorded at $\lambda = 320$ nm. SOTS-1 (8 mM) was directedly added to reaction mixtures, which were incubated with the superoxide scavenger tempol (10 mM) in advance. **c**, HPLC profiles of the Xox system (312 μM per 5 mU) restoration of tempol-inhibited $EasC_{Cf}$ activity. HPLC profiles were recorded at $\lambda = 320$ nm. The Xox system was directedly added to the EasC reaction mixtures, which were incubated with the superoxide scavenger tempol (10 mM) in advance. **d**, HRMS of CC isolated from the competitive incorporation experiment with ^{18}O-superoxide. ^{18}O-labelled CC $[M + H]^+$ *m/z*: calculated 259.1696 and observed 259.1689. The blue line displays the data for the control group without the addition of ^{18}O-superoxide, whereas the red line displays the data for the experimental group with the addition of O^{18}-superoxide. This diagram shows the relative abundance of each component, with the molecular weight of 257 set as 100%. EasC noted in the figure is $EasC_{Cf}$.

PCC and haem, respectively, through mutational study, highest occupied molecular orbital (HOMO) and spin density calculation. Mutants of these residues, including M130A, F131A and F132A, showed a significant reduction in enzyme activity (Extended Data Fig. 8a), with their protein conformation remaining unchanged (Supplementary Fig. 13). Consistent with this, theoretical calculation on frontier orbitals and spin density of the $EasC_{Cf}$–PCC binding model showed that indole nitrogen, which is close to M130, is the primary electron-donating functional group (Supplementary Figs. 14 and 15 and Supplementary Tables 4 and 5). The results were also examined by Hamiltonians to research large molecules (HARLEM) analysis[34], which confirmed the transfer of electron from the indole nitrogen of PCC to haem through M130 and F131 (Supplementary Fig. 16a). Variant F132A also exhibited lower activity than the wild-type enzyme, despite F132 being slightly off the electron transfer pathway. Structural inspection indicates that the phenyl side chain of F132 was T-stacked onto the F131 side chain, which may stabilize the position of F131 and maintain the integrity of the electron transfer pathway (Supplementary Fig. 16b). In conclusion, we proposed a similar mechanism to that of KatG[23], where the binding of O_2 is coupled with electron transfer from the indole nitrogen of PCC to haem through relay amino acids M130, F131, F132 and so on[23] (Extended Data Fig. 8c).

Superoxide mediates the cooperative catalysis

PCC binds in the NADPH-binding pocket, situated 20.6 Å from the haem centre (Fig. 2c), which is too distant and misaligned for direct interactions with Cpd III, making direct metal-oxo-mediated transformation inapplicable to the EasC reaction[8]. For comparison, in tryptophan dioxygenase, the indole ring of tryptophan is positioned just 3.5 Å above the haem[35]. Consequently, we propose a mechanism involving free ROS-mediated cooperative catalysis of the two distant pockets (Fig. 5). In this mechanism, certain ROS generated by Cpd III in the haem pocket are probably directed through the tunnel to the NADPH-binding pocket, where they mediate substrate transformation. This hypothesis is consistent with (1) the proposed ROS transfer function of the tunnel (Fig. 2d,e) and (2) the main channel being too narrow for substrate and product entry (Extended Data Fig. 2). Because Cpd III decomposition naturally generates superoxide ($O_2^{\bullet-}$; Fig. 5), superoxide was our main focus of investigation. We first excluded the involvement of singlet

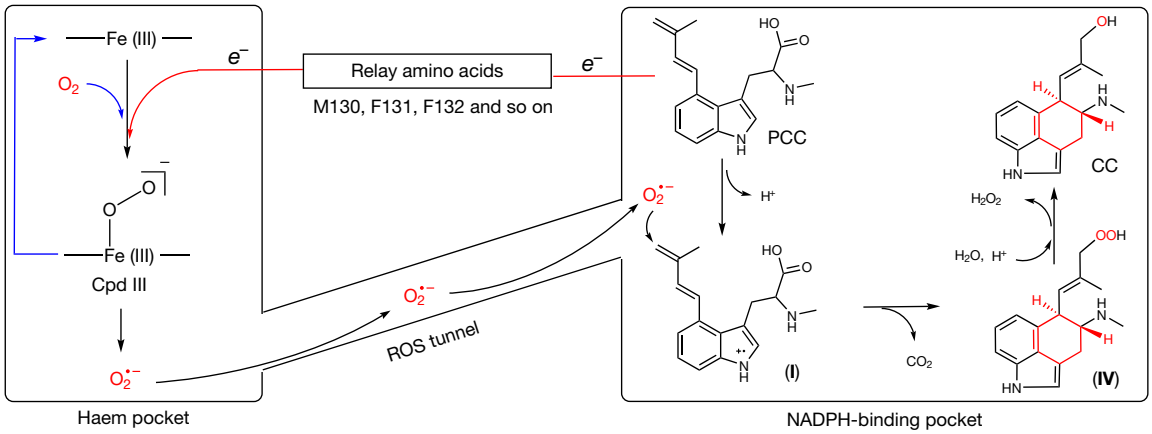

Fig. 5 | Proposed superoxide mechanism for EasC reaction. See Extended Data Fig. 8c for the details of superoxide-catalysed conversion of intermediate I–III in Fig. 5.

oxygen ($^1O_2$) by performing the $EasC_{Cf}$ reaction in the absence of light (Supplementary Fig. 17). Because ROS are short-lived and cannot be observed in $EasC_{Cf}$ structures, we explored the involvement of different ROS by adding ROS scavengers to the $EasC_{Cf}$ reaction. Most of the scavengers exhibited strong inhibitory effects (Supplementary Table 3). Bilirubin was the most potent inhibitor, with a concentration-dependent effect. At 2 mM, it caused over 70% inhibition (Extended Data Fig. 9a). The hydroxyl radical (HO•) scavenger mannitol had no significant effect (Extended Data Fig. 9b), whereas the superoxide scavenger tempol showed potent inhibition, with 1.56 mM causing about 80% inhibition (Fig. 4a). The removal of tempol by buffer exchange restored enzymatic activity (Extended Data Fig. 9c). Similarly, thiourea, another superoxide scavenger, achieved more than 80% inhibition at a concentration of 100 mM (Extended Data Fig. 9d).

We further tested the role of superoxide by adding it directly to the $EasC_{Cf}$ reactions, which were inhibited by tempol, using 4,4′-[azobis(oxymethylene)bis-benzoic acid (SOTS-1)[36] and xanthine and xanthine oxidase (Xox)[37] as superoxide sources. Both attempts restored $EasC_{Cf}$ activity (Fig. 4b,c). Given that hydroxyl radicals can oxidize nearly all amino acids[38], it is unlikely that they traverse the tunnel between the two pockets. By contrast, the less reactive superoxide reacts only with amino acids containing reactive radicals[39]. Because of its milder reactivity, superoxide plays crucial roles in various chemical and biological systems, including organic synthesis[40].

To further confirm the involvement of superoxide in the $EasC_{Cf}$ reaction, we designed a competitive incorporation experiment using ^{18}O-labelled superoxide. On the basis of our proposal, O_2 is essential for reaction initiation, and superoxide is already generated in situ from the decomposition of Cpd III (Fig. 5). Thus, the experiment involved competition between artificially introduced ^{18}O-superoxide and in situ-generated superoxide (Extended Data Fig. 10b). We performed the EasC reaction in phosphate buffer containing ^{18}O-superoxide under aerobic conditions (details in Extended Data Fig. 10c). Compared to the control group without ^{18}O-superoxide, liquid chromatography–high-resolution mass spectrometry (LC–HRMS) clearly indicates a significant enhancement in the mass spectrometry of 259 (Fig. 4d), which is two units more than the molecular weight of CC, confirming the incorporation of an oxygen atom of ^{18}O-superoxide into the final product CC. Identification of superoxide as the reactive intermediate further supports the Cpd III pathway in the EasC reaction (Fig. 3a).

Proposed mechanism for EasC reaction

We have been working to establish a superoxide mechanism for EasC (Fig. 5), where PCC in the NADPH-binding pocket donates an electron to Fe(III) in the haem pocket for O_2 reduction to generate Cpd III. Cpd III can then decompose to produce a superoxide. The generated superoxide was guided through the tunnel into the NADPH-binding pocket to mediate radical oxidative cyclization. The electron donation of indole nitrogen generates intermediate **I** with a radical cation (Extended Data Fig. 8c). **I** was further catalysed by the superoxide to generate **II**, which could reach equilibrium with **III** with a radical at C10. Consistent with this, EasC binds PCC by orienting its C4 alkyl group towards the tunnel (Fig. 2e), facilitating the attack of superoxide to the C4 alkyl group. The hydroperoxide radical in **III** could mediate the hydrogen abstraction of the carboxylic acid group to initiate decarboxylation and subsequent ring cyclization by radical coupling between C5 and C10 to generate **IV** (Extended Data Fig. 8c). Structure analysis confirmed that the distance between the terminal alkene and the hydroxyl of the carboxylic acid group in PCC was only 6.6 Å (Fig. 2e). From **IV**, the subsequent elimination of H_2O_2, detected by a H_2O_2-selective sensor (Supplementary Fig. 19), led to the formation of CC, aided by hydrogen bond interactions between the hydroperoxide group of **II** and the surrounding amino acid residues.

Discussion

Haem enzymes are among the most abundant and versatile biocatalysts in nature and are capable of performing a variety of oxidation reactions. They are found in nearly all organisms and have essential roles in many cellular events, including drug metabolism (P450s)[41], respiration (haem–copper oxidases)[42] and cellular signalling (nitric oxide synthases)[43]. In this study, we presented the structure of $EasC_{Cf}$ from the biosynthetic pathway of clinically important ergot alkaloids, revealing a dedicated superoxide mechanism. In contrast to known haem enzymes[44–46] that typically use an iron–oxygen intermediate species (Cpd I, II and III) to activate and finalize reactions, EasC uses superoxide, generated from Cpd III decomposition, to mediate the cooperative catalysis of two distant pockets. In this mechanism, free superoxide, which is relatively mild compared with hydroxyl radicals, can shuttle between two different pockets, enabling seamless cooperation. Additionally, the substrate no longer needs to directly interact with the metal centre and O_2, with O_2 activation and substrate transformation occurring in separate pockets. This separation not only substantially expands the three-dimensional space for substrate transformation but also allows for the precise regulation of multistep radical oxidative cyclization. In conclusion, the specialized functional cooperation of two distant pockets provides the structural basis for the new superoxide mechanism, enabling EasC to carry out such a complex oxidative-cyclization reaction in the biosynthesis of medicinal ergot alkaloids.

Online content

Any methods, additional references, Nature Portfolio reporting summaries, source data, extended data, supplementary information, acknowledgements, peer review information; details of author contributions and competing interests; and statements of data and code availability are available at https://doi.org/10.1038/s41586-025-08670-3.

1. Liu, H. & Jia, Y. Ergot alkaloids: synthetic approaches to lysergic acid and clavine alkaloids. *Nat. Prod. Rep.* **34**, 411–432 (2017).
2. Schiff, P. L. Ergot and its alkaloids. *Am. J. Pharm. Educ.* **70**, 98 (2006).
3. Sharma, N., Sharma, V., Manikyam, H. & Krishna, A. Ergot alkaloids: a review on therapeutic applications. *Eur. J. Med. Plants* **14**, 1–17 (2016).
4. Yao, Y. et al. Catalase involved in oxidative cyclization of the tetracyclic ergoline of fungal ergot alkaloids. *J. Am. Chem. Soc.* **141**, 17517–17521 (2019).
5. Jennings, M. E., Schaff, C. W., Horne, A. J., Lessner, F. H. & Lessner, D. J. Expression of a bacterial catalase in a strictly anaerobic methanogen significantly increases tolerance to hydrogen peroxide but not oxygen. *Microbiology* **160**, 270–278 (2014).
6. Nandi, A., Yan, L.-J., Jana, C. K. & Das, N. Role of catalase in oxidative stress- and age-associated degenerative diseases. *Oxid. Med. Cell. Longevity* **2019**, 9613090 (2019).
7. Chen, K. L. et al. Enzyme-catalyzed azepinoindole formation in clavine alkaloid biosynthesis. *Org. Lett.* **22**, 3302–3306 (2020).
8. Poulos, T. L. Heme enzyme structure and function. *Chem. Rev.* **114**, 3919–3962 (2014).
9. Tabushi, I. & Koga, N. Oxygen activation: participation of metalloenzymes and related metal complexes. *Adv. Chem. Ser.* **191**, 291–306 (1980).
10. Atanasov, A. G., Zotchev, S. B., Dirsch, V. M. International Natural Product Sciences Taskforce & Supuran, C. T. Natural products in drug discovery: advances and opportunities. *Nat. Rev. Drug Discov.* **20**, 200–216 (2021).
11. Tasker, N. R. & Wipf, P. in *The Alkaloids: Chemistry and Biology* Vol. 85 (eds Knölker, H.-J.) 1–112 (Academic, 2021).
12. Oldham, M. L., Brash, A. R. & Newcomer, M. E. The structure of coral allene oxide synthase reveals a catalase adapted for metabolism of a fatty acid hydroperoxide. *Proc. Natl Acad. Sci. USA* **102**, 297–302 (2005).
13. Putnam, C. D., Arvai, A. S., Bourne, Y. & Tainer, J. A. Active and inhibited human catalase structures: ligand and NADPH binding and catalytic mechanism. *J. Mol. Biol.* **296**, 295–309 (2000).
14. Reid, T. J. III et al. Structure and heme environment of beef liver catalase at 2.5 Å resolution. *Proc. Natl Acad. Sci. USA* **78**, 4767–4771 (1981).
15. Dong, C. et al. Tryptophan 7-halogenase (PrnA) structure suggests a mechanism for regioselective chlorination. *Science* **309**, 2216–2219 (2005).
16. Goyal, M. M. & Basak, A. Hydroxyl radical generation theory: a possible explanation of unexplained actions of mammalian catalase. *Int. J. Biochem. Mol. Biol.* **3**, 282–289 (2012).
17. Ogura, Y., Tonomura, Y., Hino, S. & Tamiya, H. Studies on the reaction between catalase molecule and various inhibitory substances, I. *J. Biochem.* **37**, 153–177 (1950).
18. Jakopitsch, C., Wanasinghe, A., Jantschko, W., Furtmueller, P. G. & Obinger, C. Kinetics of interconversion of ferrous enzymes, compound II and compound III, of wild-type *Synechocystis* catalase-peroxidase and Y249F: proposal for the catalatic mechanism. *J. Biol. Chem.* **280**, 9037–9042 (2005).
19. Wariishi, H. & Gold, M. H. Lignin peroxidase compound III. Mechanism of formation and decomposition. *J. Biol. Chem.* **265**, 2070–2077 (1990).
20. Ghiladi, R. A., Medzihradszky, K. F. & Ortiz de Montellano, P. R. Role of the Met-Tyr-Trp cross-link in *Mycobacterium tuberculosis* catalase-peroxidase (KatG) as revealed by KatG(M255I). *Biochemistry* **44**, 15093–15105 (2005).
21. Denisov, I. G., Makris, T. M., Sligar, S. G. & Schlichting, I. Structure and chemistry of cytochrome P450. *Chem. Rev.* **105**, 2253–2277 (2005).
22. Berglund, G. I. et al. The catalytic pathway of horseradish peroxidase at high resolution. *Nature* **417**, 463–468 (2002).
23. Vidossich, P., Carpena, X., Loewen, P. C., Fita, I. & Rovira, C. Oxygen binding to catalase-peroxidase. *J. Phys. Chem. Lett.* **2**, 196–200 (2011).
24. Benecky, M. J., Frew, J. E., Scowen, N., Jones, P. & Hoffman, B. M. EPR and ENDOR detection of compound I from *Micrococcus lysodeikticus* catalase. *Biochemistry* **32**, 11929–11933 (1993).
25. Jacob, G. S. & Orme-Johnson, W. H. Catalase of *Neurospora crassa*. 2. Electron paramagnetic resonance and chemical properties of the prosthetic group. *Biochemistry* **18**, 2975–2980 (1979).
26. Wood, P. M. The two redox potentials for oxygen reduction to superoxide. *Trends Biochem. Sci.* **12**, 250–251 (1987).
27. Bandara, D. M. I., Sono, M., Bruce, G. S., Brash, A. R. & Dawson, J. H. Coordination modes of tyrosinate-ligated catalase-type heme enzymes: magnetic circular dichroism studies of *Plexaura homomalla* allene oxide synthase, *Mycobacterium avium ssp. paratuberculosis* protein-2744c, and bovine liver catalase in their ferric and ferrous states. *J. Inorg. Biochem.* **105**, 1786–1794 (2011).
28. Kracher, D. et al. Extracellular electron transfer systems fuel cellulose oxidative degradation. *Science* **352**, 1098–1101 (2016).
29. Farver, O., Wherland, S. & Pecht, I. Intramolecular electron transfer in ascorbate oxidase is enhanced in the presence of oxygen. *J. Biol. Chem.* **269**, 22933–22936 (1994).
30. Brunori, M., Antonini, G., Malatesta, F., Sarti, P. & Wilson, M. T. The oxygen reactive species of cytochrome-c-oxidase: an alternate view. *FEBS Lett.* **314**, 191–194 (1992).
31. Wang, Z., Feng, S., Rovira, C. & Wang, B. How oxygen binding enhances long-range electron transfer: lessons from reduction of lytic polysaccharide monooxygenases by cellobiose dehydrogenase. *Angew. Chem. Int. Ed.* **60**, 2385–2392 (2021).
32. Giese, B. et al. Electron relay race in peptides. *J. Org. Chem.* **74**, 3621–3625 (2009).
33. Cordes, M. et al. Influence of amino acid side chains on long-distance electron transfer in peptides: electron hoping via "stepping stones". *Angew. Chem. Int. Ed.* **47**, 3461–3463 (2008).
34. Kurnikov, I. V. *HARLEM Molecular Modeling Package* (Department of Chemistry, Univ. of Pittsburgh, 2000).
35. Forouhar, F. et al. Molecular insights into substrate recognition and catalysis by tryptophan 2,3-dioxygenase. *Proc. Natl Acad. Sci. USA* **104**, 473–478 (2007).
36. Heller, M. I. & Croot, P. L. Application of a superoxide (O_2^-) thermal source (SOTS-1) for the determination and calibration of O_2^- fluxes in seawater. *Anal. Chim. Acta* **667**, 1–13 (2010).
37. Shibuya, S., Watanabe, K., Ozawa, Y. & Shimizu, T. Xanthine oxidoreductase-mediated superoxide production is not involved in the age-related pathologies in Sod1-deficient mice. *Int. J. Mol. Sci.* **22**, 3542 (2021).
38. Xu, G. & Chance, M. R. Hydroxyl radical-mediated modification of proteins as probes for structural proteomics. *Chem. Rev.* **107**, 3514–3543 (2007).
39. Carroll, L. et al. Superoxide radicals react with peptide-derived tryptophan radicals with very high rate constants to give hydroperoxides as major products. *Free Radic. Biol. Med.* **118**, 126–136 (2018).
40. Hayyan, M., Hashim, M. A. & AlNashef, I. M. Superoxide ion: generation and chemical implications. *Chem. Rev.* **116**, 3029–3085 (2016).
41. Zanger, U. M. & Schwab, M. Cytochrome P450 enzymes in drug metabolism: regulation of gene expression, enzyme activities, and impact of genetic variation. *Pharmacol. Ther.* **138**, 103–141 (2013).
42. Garcia-Horsman, J. A., Barquera, B., Rumbley, J., Ma, J. & Gennis, R. B. The superfamily of heme-copper respiratory oxidases. *J. Bacteriol.* **176**, 5587–5600 (1994).
43. Tuteja, N., Chandra, M., Tuteja, R. & Misra, M. K. Nitric oxide as a unique bioactive signaling messenger in physiology and pathophysiology. *J. Biomed. Biotechnol.* **2004**, 227–237 (2004).
44. Gao, S.-S., Naowarojna, N., Cheng, R., Liu, X. & Liu, P. Recent examples of α-ketoglutarate-dependent mononuclear non-haem iron enzymes in natural product biosyntheses. *Nat. Prod. Rep.* **35**, 792–837 (2018).
45. McIntosh, J. A., Farwell, C. C. & Arnold, F. H. Expanding P 450 catalytic reaction space through evolution and engineering. *Curr. Opin. Chem. Biol.* **19**, 126–134 (2014).
46. Tang, M.-C., Zou, Y., Watanabe, K., Walsh, C. T. & Tang, Y. Oxidative cyclization in natural product biosynthesis. *Chem. Rev.* **117**, 5226–5333 (2017).

Methods

Plasmid construction, protein expression, purification and in vitro assays

To construct plasmids for protein expression of EasC from *C. fusiformis* ($EasC_{Cf}$; GenBank no. ABV57821.1) and *A. fumigatus* ($EasC_{Af}$; GenBank accession no. XM_751047.1), the DNA fragments were amplified using the corresponding primers and inserted into *Nde*I- and *Xho*I-digested pET28a using the Gibson assembly method. The plasmids for enzyme mutants were constructed by amplifying the wild-type template using corresponding primers by means of a fast mutagenesis system kit. The primers used are listed in Supplementary Table 1. The plasmids were transformed into *Escherichia coli* BL21(DE3) competent cells for protein expression. Precultures were grown overnight in Luria–Bertani (LB) medium (10 ml) containing 50 μg ml^{-1} of kanamycin at 37 °C with shaking at 250 rpm. Then, 10 ml of preculture was transferred to 1 l of fresh LB medium with 50 μg ml^{-1} of kanamycin and further incubated at 37 °C with shaking at 250 rpm. When the optical density at 600 nm reached 0.6–0.8, the expression of EasC was induced by 5 μM isopropyl β-D-thiogalactopyranoside supplemented with 10 μM chlorhematin (chlorohemin or chloroprotoporphyrin IX iron(III)) and cultured for 18 h at 16 °C and 200 rpm. Cells were collected by centrifugation at 5,000 rpm for 30 min and suspended in buffer A containing 25 mM Tris-HCl (pH 7.5), 150 mM NaCl and 20 mM imidazole, followed by disruption using a French press (JuNeng Biology & Technology). The cell lysate was centrifuged at 4 °C for 50 min at 17,000*g* to remove the cell debris. The supernatant was applied to a fast protein liquid chromatography system (GE HealthCare) coupled with a Ni–NTA column and eluted with a gradient of 20–500 mM imidazole in buffer A. Purified proteins were dialysed and concentrated to 10 mg ml^{-1} in buffer A without imidazole. The SDS–PAGE analyses of the wild-type and variant $EasC_{Cf}$ proteins are shown in Supplementary Fig. 18.

A typical 50 μl of the assay solution containing 50 mM Tris-HCl buffer (pH 7.5), 40–100 μM enzymes, 2 mM NADPH and 0.5 mM substrate was prepared for testing the enzymatic activities of EasC. The reactions were generally performed at 30 °C for 1 h and quenched by adding 100 μl of methanol. Protein precipitate from the reactions was removed by centrifugation. The supernatant was then analysed using HPLC and liquid chromatography–mass spectrometry (LC–MS). The enzyme activity of each mutant was calculated as a percentage of wild-type enzyme, which was set at 100%.

Protein purification, cryo-EM data acquisition and processing, model building and refinement of $EasC_{Cf}$

To solve the protein structure, the protein solution of $EasC_{Cf}$ obtained by performing the aforementioned procedure was further purified through size exclusion chromatography coupled with a Superdex 200 10/300 GL column (GE HealthCare). Peak fractions were collected for cryo-EM sample preparation. For complex structure, the recombinant $EasC_{Cf}$ protein was incubated with 10 mM PCC for 30 min before cryo-sample preparation.

To prepare cryo-EM samples, 4 μl of purified $EasC_{Cf}$ (0.5 mg ml^{-1}) or substrate-engaged $EasC_{Cf}$ (0.5 mg ml^{-1}) was applied onto glow-discharged holey carbon grids (Quantifoil Cu R1.2/1.3; 300 mesh). The grids were then blotted for 5 s at 4 °C with 100% humidity and plunge frozen in liquid ethane cooled by liquid nitrogen using a Vitrobot Mark IV (Thermo Fisher Scientific). High-quality grids were loaded onto a Titan Krios electron microscope, operated at 300 kV, for data collection. Image stacks were recorded with a K3 detector (Gatan) using EPU (Thermo Fisher Scientific) in super-resolution counting mode at a nominal magnification of 105,000× corresponding to a calibrated pixel size of 0.425 Å. Each stack of 40 frames was exposed for 2.5 s with preset defocus values ranging from −1.0 to −2.4 μm, and the total dose for each stack was approximately 52 $e^{-}/Å^{2}$.

All cryo-EM data processing was performed using CryoSPARC v.3.3.1 (ref. 47). In general, the video stacks were motion-corrected using patch motion correction, and the micrographs were binned to 0.85 Å per pixel. These images were used for contrast transfer function estimation using a patch-based contrast transfer function. For apo-form $EasC_{Cf}$, a total of 1,002 good micrographs were selected, and 590,067 particles were automatically picked using the CryoSPARC Blob Picker and extracted with a box size of 256 pixels. After two rounds of two-dimensional classification, 296,958 particles were selected, followed by one round of ab initio reconstruction. The dataset was processed with C1 and C2 symmetries, which yielded similar maps and models. Thus, C2 symmetry was applied in subsequent analyses. Particles were subjected to one round of heterogeneous refinement on the basis of two better classes to further remove bad particles. After one round of non-uniform and local refinement, a final dataset of 184,130 particles was reconstructed to produce a 2.64 Å resolution map (Supplementary Fig. 3). The substrate-engaged $EasC_{Cf}$ data were processed using the same workflow. A total of 2,027 good micrographs were selected, and 1,155,245 particles were picked automatically. After two rounds of two-dimensional classification, 839,745 particles were selected for one round of ab initio reconstruction. Similar to the case for the apo-form $EasC_{Cf}$, maps were generated using C1 and C2 symmetries. C2 symmetry was applied to produce the final maps. After one round of heterogeneous refinement and one round of non-uniform and local refinement, a final dataset of 603,385 particles was reconstructed to produce a 2.33 Å resolution map (Supplementary Fig. 4). All maps were subjected to a sharpening process using the Sharpening Tools in CryoSPARC, and the resolution of the final maps was estimated by gold-standard Fourier shell correlation using the 0.143 criterion.

The atomic model of apo-form $EasC_{Cf}$ built using AlphaFold2 (ref. 48) was docked into the apo-form $EasC_{Cf}$ map in UCSF Chimera[49]. The model was manually adjusted in Coot v.0.9.6 (ref. 50), followed by refinement against the corresponding map using the phenix.real_space_refine program in Phenix v.1.20 with geometry and secondary structure restraints imposed[51]. The model of substrate-engaged $EasC_{Cf}$ was built starting with the model of the apo-form $EasC_{Cf}$. All final models were evaluated using MolProbity[52]. The statistics of map reconstruction and model building are summarized in Supplementary Table 2.

HPLC and LC–MS analysis

The conversion of biochemical reactions was calculated according to the relative peak area of the substrate analysed using HPLC or LC–MS at a UV detection wavelength of 320 nm (for PCC).

For method A, samples were analysed by Waters 2596 equipped with a mass spectrum detector (2996) and a C18 column (Agilent Eclipse XDB-C18; 2.1 × 100 mm; 3.5 μm) and eluted with a gradient method (0–100% mobile phase B in 15 min, with H_2O and MeCN as mobile phases A and B, respectively) using a flow rate of 0.3 ml min^{-1}. For method B, samples were analysed by CORUI HPLC system equipped with a C18 analytic column (Agilent Eclipse Plus C18; 4.6 × 250 mm; 5.0 μm) and eluted with a gradient method (0–100% mobile phase B in 20 min, with H_2O and MeCN as mobile phases A and B, respectively) using a flow rate of 1.0 ml min^{-1}.

Molecular docking

Molecular docking was performed using the CDOCKER procedure in Discovery Studio Client v.19.1.0.

NaN_3 and NH_2OH inhibitory assay

To test the inhibitory effect of NaN_3 and NH_2OH on $EasC_{Cf}$, we prepared a 50-μl reaction solution consisting of 50 mM Tris-HCl buffer (pH 7.5), 40 μM enzymes, 0.5 mM substrate, 2 mM NADPH and several concentrations of sodium azide (320→0.039 mM) and hydroxylamine (25→0.006 mM). The reactions were incubated for 1 h at 30 °C and quenched with 100-μl methanol. Proteins in the reactions were removed

by centrifugation. The supernatant was then analysed using LC–MS. Inhibition potency (IC_{50}) values were calculated using a four-parameter logistic equation using GraphPad Prism, v.6.0 (GraphPad Software). Percentage of inhibition = (substrate residual rate with inhibitors − substrate residual rate without inhibitors) × 100%.

ROS inhibitory assay

To evaluate the ROS inhibitory effect, we prepared a 50-µl reaction solution that included 50 mM Tris-HCl buffer (pH 7.5), 40 µM enzymes, 0.5 mM substrate, 2 mM NADPH and different concentrations of scavengers. The reactions were implemented for 1 h at 30 °C and then quenched with 100 µl methanol. Proteins in the reactions were removed by centrifugation. The supernatant was then analysed by LC–MS. The enzyme activity of each sample was calculated as a relative value, with the activity in the absence of inhibitors set at 100%

Superoxide generation assay for EasC activity restoration

For in vitro studies, we prepared a 50-µl reaction solution containing 50 mM Tris-HCl buffer (pH 7.5), 20 µM enzymes, 0.5 mM substrate, 2 mM NADPH, 10 mM tempol and different concentrations of superoxide generators. The reactions were performed for 3 h at 30 or 37 °C and then quenched with 100 µl methanol, and the supernatant was analysed using LC–MS.

For in vivo studies, 100 ml of culture was inoculated with a preculture (1 ml) of *E. coli* BL21(DE3) expressing $EasC_{Cf}$. Protein expression was induced by 5 µM isopropyl β-D-thiogalactopyranoside. The cells were then collected by centrifugation at 5,000 rpm for 10 min and resuspended in a fresh LB medium (5 ml) containing 50 µg ml^{-1} of kanamycin. Each 50-µl reaction contained 40 µl cell suspension, 0.5 mM substrate, 2 mM NADPH, 240 mM Thiourea and different concentrations of plumbagin and clofazimine. The mixtures were incubated at 30 °C for 12 h and quenched with 100 µl methanol. The resultant supernatant was analysed using HPLC.

ITC tests

MicroCal iTC200 was used for the characterization of the interaction between $EasC_{Cf}$ and PCC. $EasC_{Cf}$ was diluted in an ITC buffer (150 mM NaCl and 20 mM Tris-HCl (pH 7.5)) to a final concentration of 20 µM. PCC and NADPH were dissolved in the ITC buffer with both in a final concentration of 200 µM. The ITC conditions were as follows: 330 µl of the enzyme was first injected into the sample cell. Titration was then initiated with a first injection of 0.4 µl of the corresponding substrate, followed by 19 injections of 2 µl at 25 °C. Blank tests were carried out using an ITC buffer instead of enzymes in the titration step and were used for baseline correction. Instrument software was used to calculate the normalized heat released from each injection.

Measurement of H_2O_2 generated in EasC reaction

OxiVision Green hydrogen peroxide sensor (AAT Bioquest) was used to quantitatively determine the H_2O_2 generated in EasC reaction according to the manufacturer's instructions. The 50-µl $EasC_{cf}$ reaction solution containing 50 mM Tris-HCl buffer (pH 7.5), 10 µM enzyme, 0.6 mM substrate and 2 mM NADPH was first incubated at 30 °C for 1 h. Then, the preprepared 50-µl sensor solution containing 20 mM HEPES buffer and 10 µM OxiVision Green H_2O_2 sensor was added into the reaction. Finally, a total of 100 µl mixture was incubated in a 96-well plate at room temperature, and fluorescence intensity was recorded at Ex/Em = 490/525 nm for 15–75 min using an EnSpire 2300 Multimode Reader (PerkinElmer). A 50-µl reaction solution without enzyme was used as the negative control; 1 mM H_2O_2 was diluted by ratio and used to prepare the standard curves of H_2O_2 according to the manufacturer's instructions.

Stopped-flow spectrophotometry

The sequential mixing stopped-flow apparatus (model SX20), equipped with a dedicated computer system and software, was sourced from Applied Photophysics. A monochromator and a diode-array detector (Applied Photophysics PD.1), integrated with the stopped-flow machine, were used to track the progress of all reactions. All measurements were conducted at 25 °C in 50 mM phosphate buffer (pH 7.5). The diode-array detector was specifically used for these measurements, and each sample was subjected to at least three independent determinations.

Under aerobic conditions, an experiment was designed to investigate whether binding of the substrate PCC to $EasC_{Cf}$ could facilitate the acquisition of electrons on the haem iron centre and subsequent oxygen binding. One syringe was loaded with 40 µM $EasC_{Cf}$ dissolved in 50 mM phosphate-buffered saline (PBS) at pH 7.5, whereas the second syringe contained 0.5 mM PCC.

To gain insights into the intermediate iron–oxygen complex formed during the $EasC_{Cf}$ reaction, a stopped-flow apparatus was harnessed to monitor UV–Vis spectral changes occurring in 1 s under aerobic conditions. In this experiment, the first syringe contained 40 µM enzyme in 50 mM PBS at pH 7.5, whereas the second syringe contained a mixed solution comprising 0.5 mM PCC.

EPR measurement

EPR spectra were acquired using a Bruker EMXplus spectrometer equipped with a helium-flow cryostat operating at a temperature of 15 K. The experimental parameters were set as follows: microwave frequency of 9.406 GHz, microwave power output of 20 mW, modulation frequency adjusted to 100 kHz and modulation amplitude of 20 G. Spectral scans were conducted over a broad range, from 5 to 505 mT.

To maintain anaerobic conditions, oxygen was removed from the buffer solutions using nitrogen displacement, and the enzymes and reagents (sodium dithionite, PCC and CC) were treated anaerobically for 3 h in a glove box. Samples were diluted to 200 µl with anaerobic buffer and transferred to EPR tubes for analysis. Four groups of samples contained 492 µM purified $EasC_{Cf}$, 442 µM $EasC_{Cf}$ and 10 mM sodium dithionite, 480 µM $EasC_{Cf}$ and 5.19 mM PCC, and 480 µM $EasC_{Cf}$ and 4.93 mM CC, respectively.

Circular dichroism measurement

Circular dichroism spectra were collected using a circular dichroism spectrometer (Chirascan; Applied Photophysics) to investigate the conformational stability of protein $EasC_{Cf}$. Far-UV spectra (spanning 180–260 nm) were recorded in a 0.1-cm path length quartz cuvette with an internal volume of 0.2 ml. The protein was diluted to a concentration of 0.967 mg ml^{-1} in 10 mM phosphate buffer at pH 7.0.

To elucidate the role of NADPH in the $EasC_{Cf}$ reaction, circular dichroism spectra were analysed for $EasC_{Cf}$ that reacted with PCC in the presence and absence of the cofactor NADPH. Specifically, the reaction mixture containing NADPH comprised 35 µM $EasC_{Cf}$, 1 mM PCC and 10 mM NADPH, whereas the mixture lacking NADPH contained only 35 µM $EasC_{Cf}$ and 1 mM PCC.

After incubating these reaction systems for 2, 4 and 8 h, the reactions were halted by transferring the systems to ice. By comparing the circular dichroism spectra obtained at these time points and under varying conditions (with or without NADPH), insights into the effect of NADPH on the conformational stability and reaction mechanism of $EasC_{Cf}$ with PCC could be gained.

O^{18}-labelled superoxide assay

To produce O^{18}-superoxide used for the $EasC_{Cf}$ reaction, 50 mM PBS buffer (pH 7.5), 2 mM NADPH and 8 mM SOTS-1 were added to an $^{18}O_2$-containing tube in a glove box. After incubation for 10 min at room temperature, 50 µl of the mixture was transferred into a 1.5-ml centrifuge tube in open air and mixed thoroughly using a vortex oscillator to release the residual $^{18}O_2$. Then, 0.6 mM PCC and 40 µM $EasC_{Cf}$ were added to the mixture, and the reaction was further performed at 30 °C for 1 h. The negative control, without SOTS-1, was prepared as described

above. The reactions were quenched with 100 µl methanol, and the supernatant was then analysed using HRMS.

Reporting summary

Further information on research design is available in the Nature Portfolio Reporting Summary linked to this article.

Data availability

All data are available in the main text, Extended Data figures or the Supplementary Information. The three-dimensional cryo-EM density maps of $EasC_{Cf}$ and $EasC_{Cf}$–PCC have been deposited in the Electron Microscopy Data Bank under accession numbers EMD-61387 and EMD-61388, respectively. The coordinates of $EasC_{Cf}$ and $EasC_{Cf}$–PCC have been deposited in the Protein Data Bank under accession codes 9JDB and 9JDC, respectively.

47. Punjani, A., Rubinstein, J. L., Fleet, D. J. & Brubaker, M. A. CryoSPARC: algorithms for rapid unsupervised cryo-EM structure determination. *Nat. Methods* **14**, 290–296 (2017).
48. Jumper, J. et al. Highly accurate protein structure prediction with AlphaFold. *Nature* **596**, 583–589 (2021).
49. Pettersen, E. F. et al. UCSF Chimera—a visualization system for exploratory research and analysis. *J. Comput. Chem.* **25**, 1605–1612 (2004).
50. Emsley, P., Lohkamp, B., Scott, W. G. & Cowtan, K. Features and development of Coot. *Acta Crystallogr. D* **66**, 486–501 (2010).
51. Afonine, P. V. et al. Real-space refinement in PHENIX for cryo-EM and crystallography. *Acta Crystallogr. D* **74**, 531–544 (2018).
52. Chen, V. B. et al. MolProbity: all-atom structure validation for macromolecular crystallography. *Acta Crystallogr. D* **66**, 12–21 (2010).

Acknowledgements This study was supported by the National Key Research and Development Program of China (grant no. 2019YFA0905100), the National Natural Science Foundation of China (grant nos. 32470074, 32371307 and 82341210), Tianjin Synthetic Biotechnology Innovation Capacity Improvement Project (grant nos. TSBICIP-CXRC-062 and TSBICIP-CXRC-069), Hubei Hongshan Laboratory (grant no. 2022hszd030), the Interdisciplinary Research Project of Hangzhou Normal University (grant no. 2024JCXK02) and the Strategic Priority Research Program of CAS (grant no. XDB0960300).

Author contributions S-S.G., R.-T.G., C.-C.C. and C.C. designed the experiments. Y.Y. collected the genes and completed the bioinformatics analysis. Z.-P.Y., Y.Y. and L. Yang performed microbial fermentation and genetic and biochemical experiments. C.C., J.B. and J.Y. prepared the compounds CC and PCC. X.S. and H.S. performed theoretical calculations. Z.L., L.Z., T.W., J.-W.H., X.L. and P.S. performed structural work. C.-C.C., Z.L., L.Z., J.-W.H., Y.M. and J.M. performed structural data management, processing and molecular docking. P.-L.H., W.Z., R.A.S., L. Yu and A.L. performed EPR data collection and analysis. S.-S.G., R.-T.G., C.-C.C., C.C. and C.-Y.W. analysed the data and wrote the article, which was edited and approved by all authors.

Competing interests The authors declare no competing interests.

Additional information

Supplementary information The online version contains supplementary material available at https://doi.org/10.1038/s41586-025-08670-3.

Correspondence and requests for materials should be addressed to Rey-Ting Guo or Shu-Shan Gao.

Peer review information *Nature* thanks Wolfgang Kroutil and the other, anonymous, reviewer(s) for their contribution to the peer review of this work. Peer reviewer reports are available.

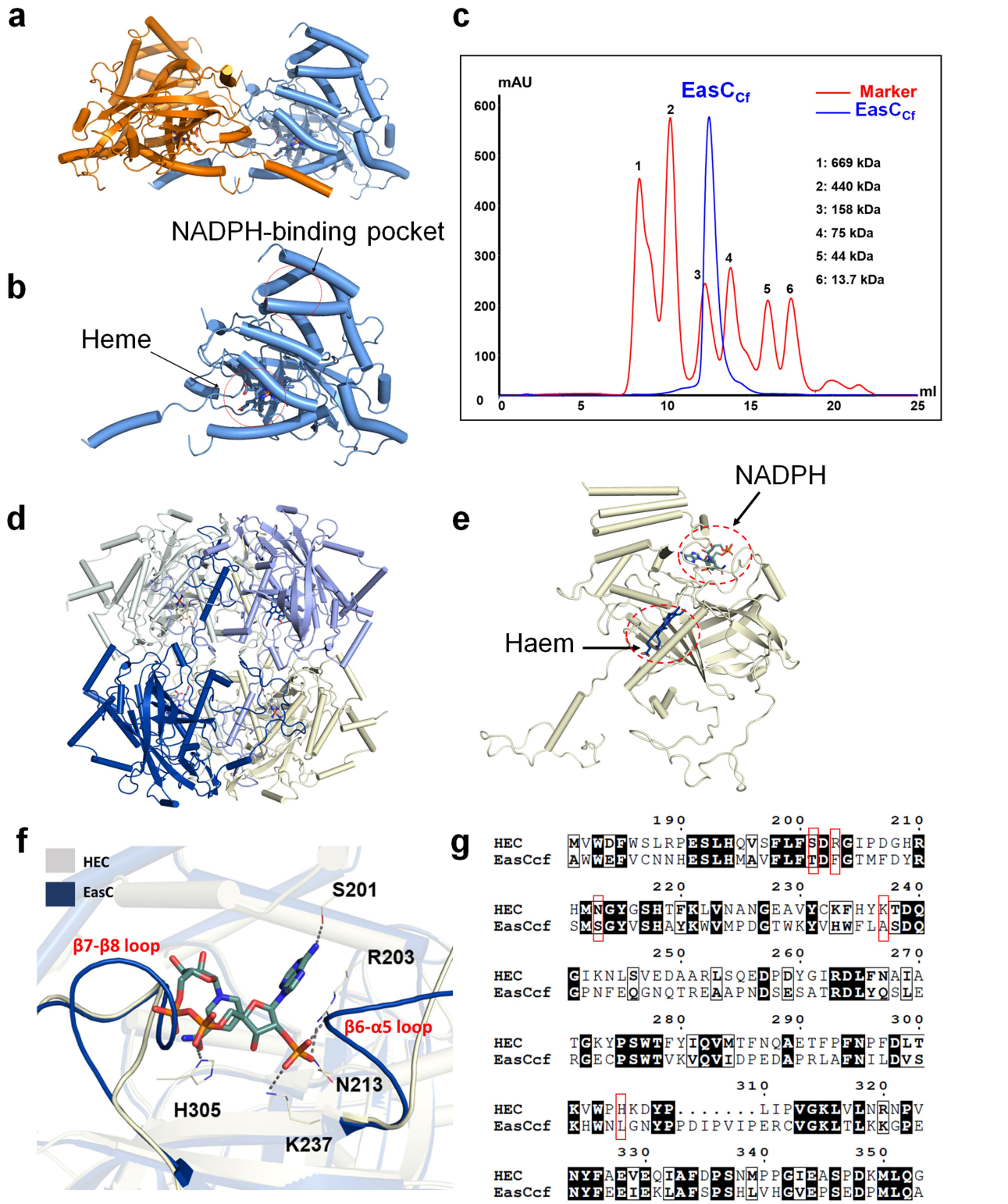

Extended Data Fig. 1 | Overall structure of EasC$_{Cf}$ and comparison to Human Erythrocyte Catalase (HEC). a, EasC$_{Cf}$'s oligomerization status. **b**, Cartoon model of EasC$_{Cf}$ monomer. No NADPH can be found in the NADPH binding pocket. **c**, The SEC analysis of EasC$_{Cf}$. The blue and red traces represent EasC$_{Cf}$ and a marker that contains six proteins with known molecular mass. The theoretical and calculated molecular mass of EasC$_{Cf}$ is 53.98 and 102.45 kDa, respectively, suggesting that EasC$_{Cf}$ should exist as a dimer in solution. **d**, HEC's oligomerization status. **e**, Cartoon model of HEC monomer. **f**, The overlay of the NADPH-binding pockets in HEC and EasC$_{Cf}$. Dashed lines indicate polar interactions with distance <3.5 Å. **g**, Sequence alignment between the amino acids forming the NADPH binding pocket in HEC and EasC$_{Cf}$, which was performed with ClustalW using MEGA11 and visualized with ENDscript 3. The red boxes indicate the residues forming hydrogen bonding interactions with the bonded NADPH in HEC and their equivalents in EasC$_{Cf}$. See Supplementary Fig. 5 for a full sequence alignment between EasC$_{Cf}$ and HEC.

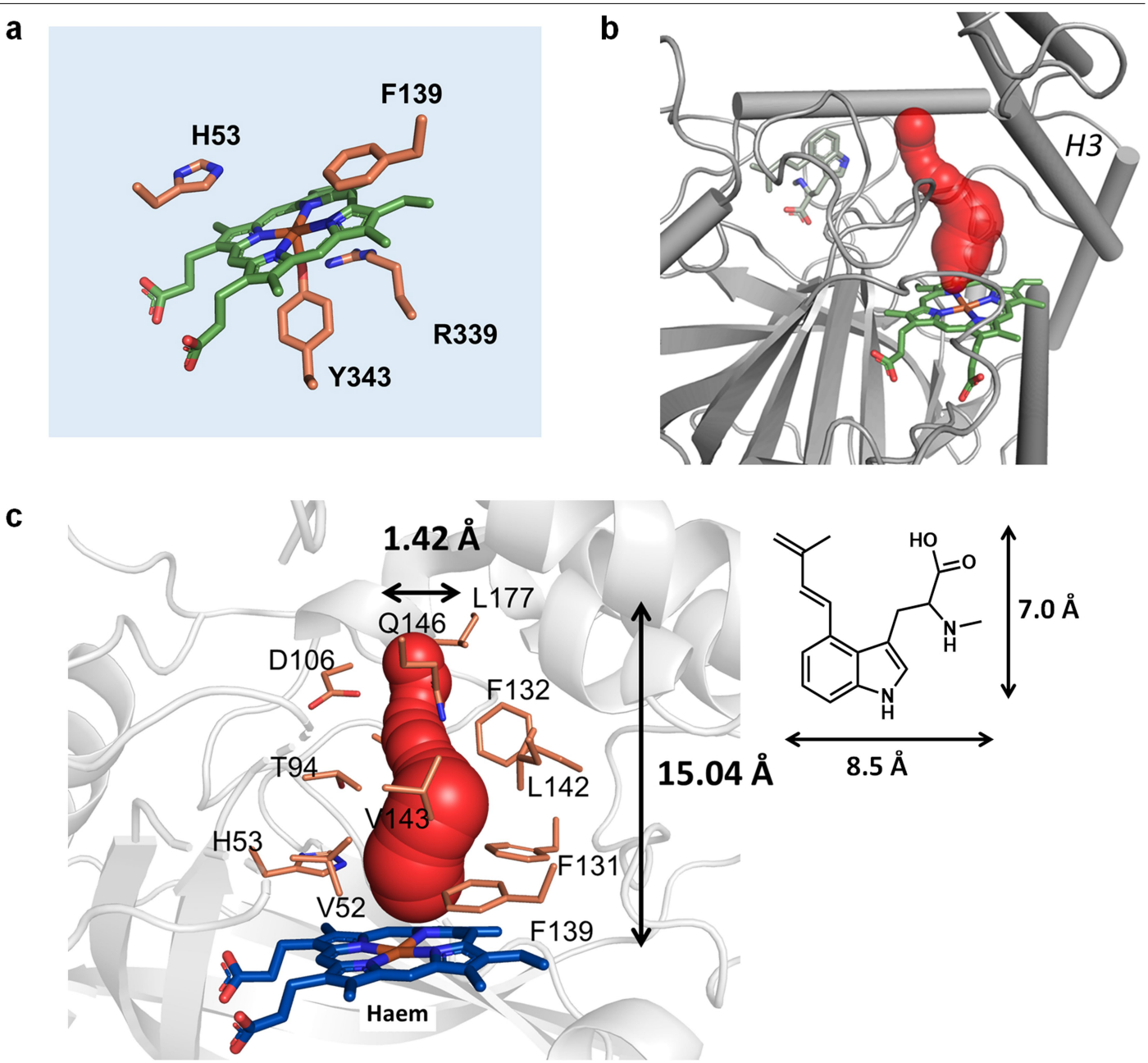

Extended Data Fig. 2 | Structure and haem environment of EasC$_{cf}$. a, Stereo diagram of the haem environment. The essential residues are Y343, the fifth coordinating ligand of the haem iron, on the proximal side and H53 on the distal side. **b**, The opening channel in the haem pocket. **c**, Key amino residues forming the opening channel. The haem group is buried at least 15 Å below the molecular surface and is accessible by the opening channel lined with hydrophobic residues. The top right corner shows the size of the substrate molecule **PCC**.

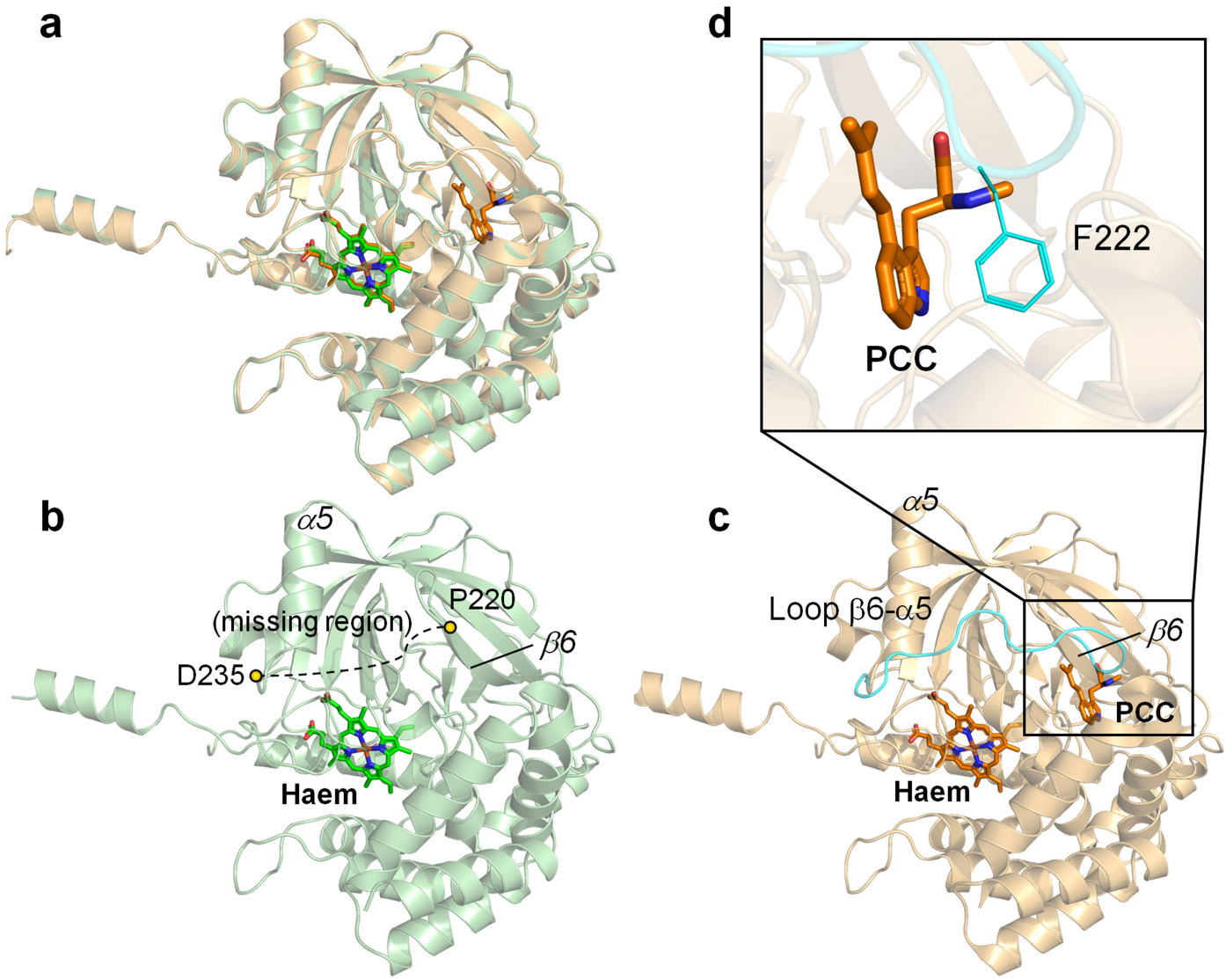

Extended Data Fig. 3 | Structural comparison of *apo*-form and PCC-bound $EasC_{Cf}$. **a**, The superimposition of apo-form (green) and **PCC**-bound $EasC_{Cf}$ (wheat). **b**, The apo-form $EasC_{Cf}$ with P220 and D235 located on either end of the missing region (dashed curve) indicated by spheres. **c**, The **PCC**-bound $EasC_{Cf}$ complex structure with loop β6-α5 indicated and colored in cyan. **d**, The zoom-in view shows T-stacking interaction between **PCC** and F222.

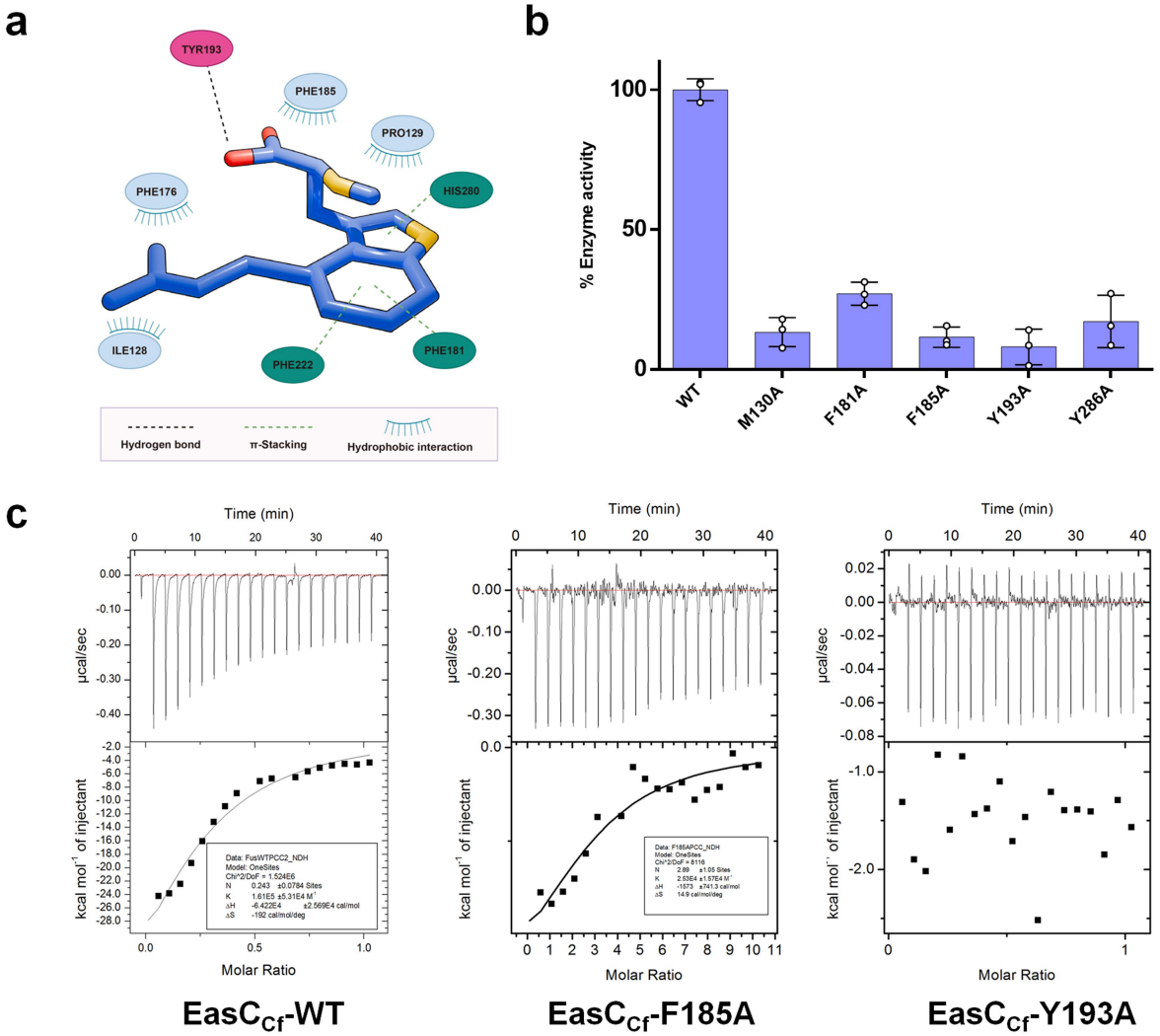

Extended Data Fig. 4 | The ligand-enzyme interactions in the NADPH binding pocket of $EasC_{Cf}$. a, Detailed interaction between **PCC** and $EasC_{Cf}$ characterized by LigandPlot. **PCC** shown in blue sticks and coloured by atom type. Polar and hydrophobic interactions were mapped with the LigPlot program and indicated with dashed lines or a starburst symbol. **b**, The mutational results of key residues of $EasC_{Cf}$. The enzyme activity of each sample is calculated as a percentage of the wild type enzyme (WT). The individual ($n = 3$) and average values along with error bars (s.d.) of each group in one representative experiment among three independent experiments are shown. **c**, ITC measurement of **PCC** binding to corresponding $EasC_{Cf}$ mutants. $EasC_{Cf}$-WT and F185A was observed to interact with **PCC**. The K_D was determined to 6.21 ± 0.19 µM and 39.5 ± 6.37 µM, respectively. Heat changes measured as a function of time at 25 °C are shown. (Lower) Normalized heat changes (filled square) and the best-fit curve (solid line) are shown.

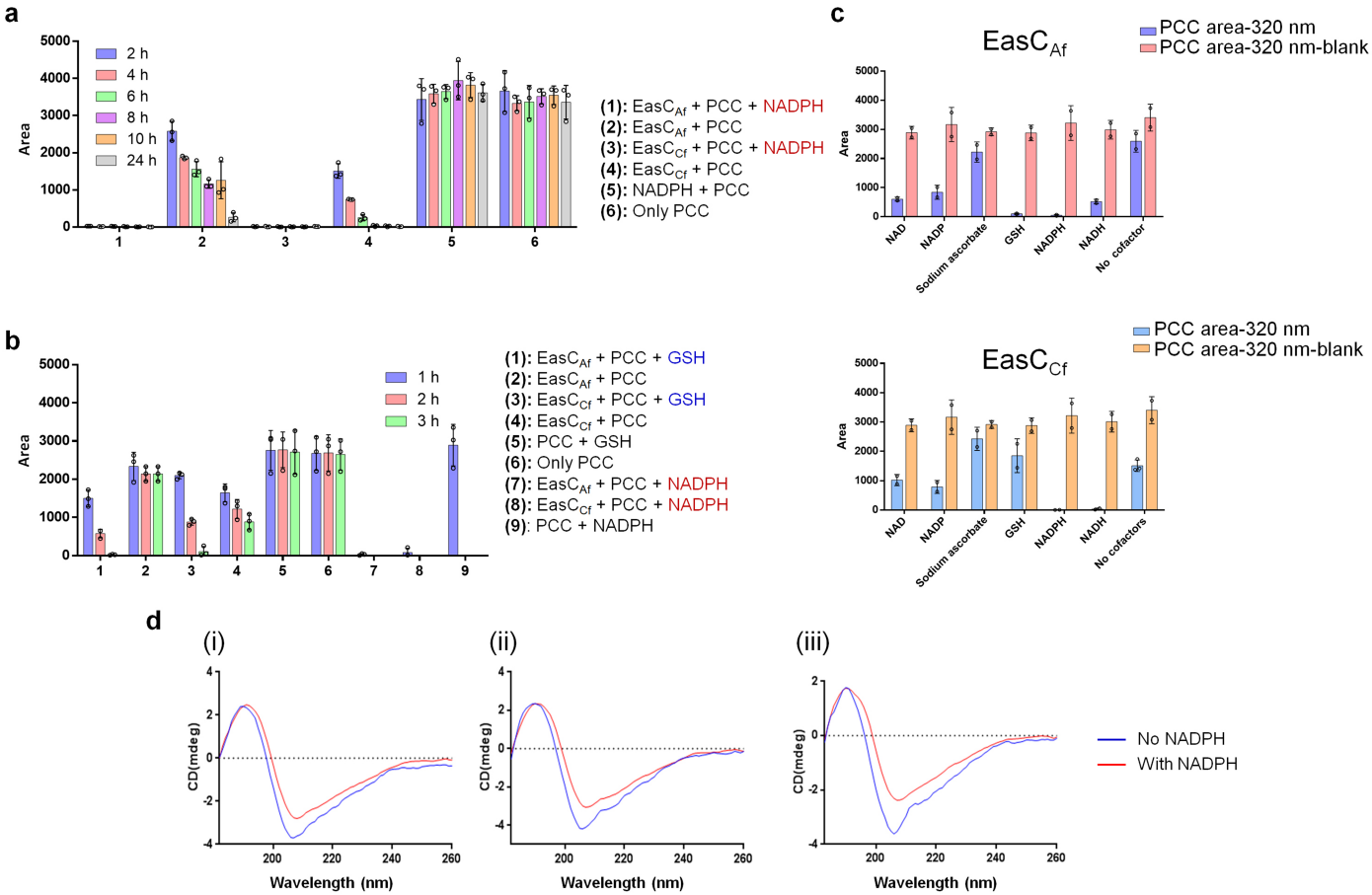

Extended Data Fig. 5 | The effects of different small molecules on the EasC-reaction. a, The residual **PCC** of the reactions catalyzed by EasC$_{Af}$ and EasC$_{Cf}$. **b**, The residual **PCC** of the EasC reactions with the addition of GSH and NADPH, respectively. Reaction details: a 50 μL typical assay solution contained 50 mM Tris-HCl buffer (pH 7.5), 40 μM enzymes, 2 mM NADPH and 1 mM substrate. **c**, The residual **PCC** of the 2 h reaction of EasC with the addition of NAD, NADP, sodium ascorbate, NADH, and NADPH, respectively. **d**, Circular dichroism (CD) spectra of the EasC$_{Cf}$ protein, extracted from reactions conducted in the presence or absence of NADPH. (i), (ii), and (iii) are CD spectra of EasC$_{Cf}$ protein isolated from 2 h, 4 h, and 8 h reaction, respectively. In **a**, **b** and **c**, individual ($n = 3$) and average values of each group along with error bars (s.d.) of one representative experiment among three independent experiments are presented.

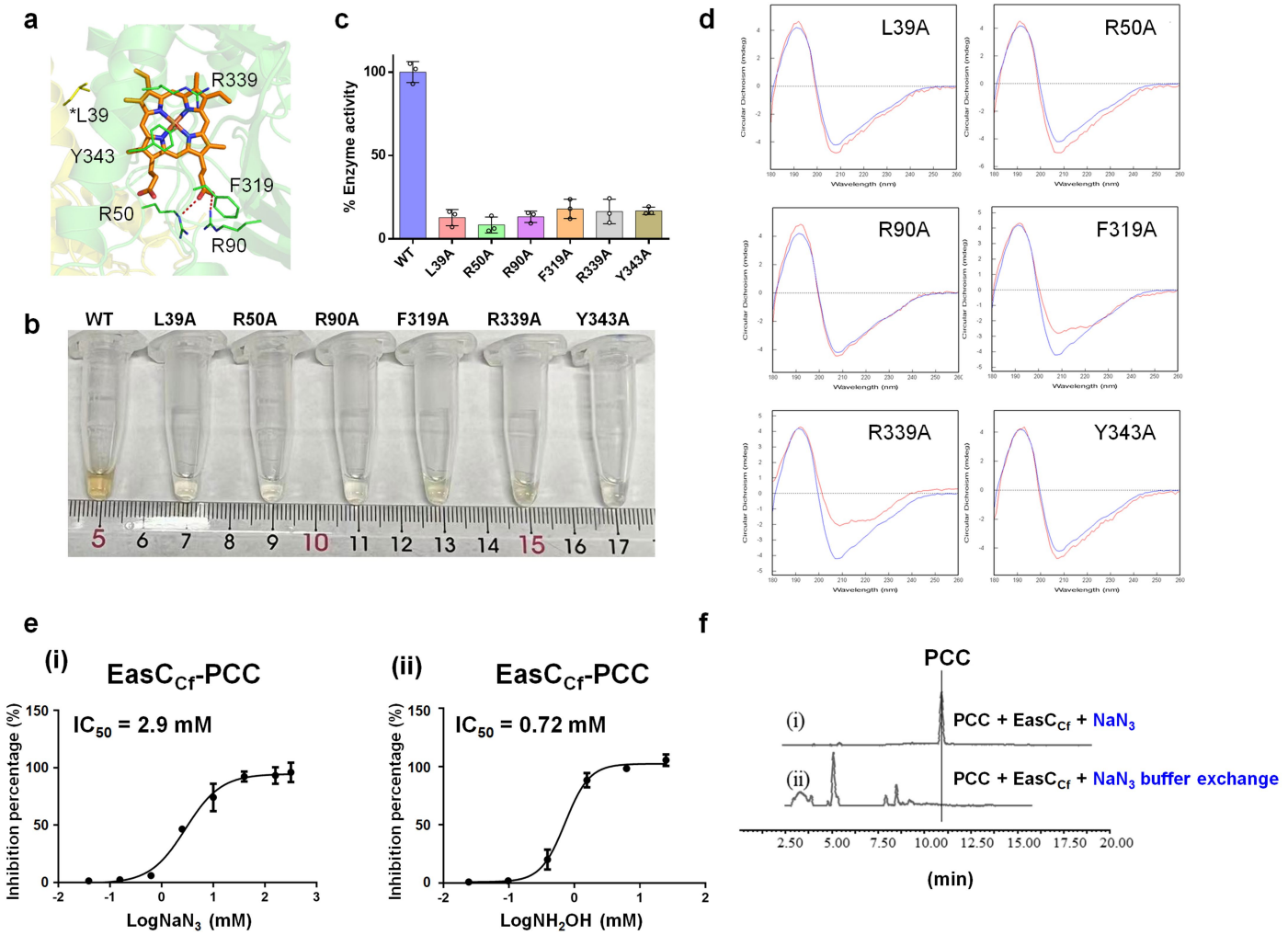

Extended Data Fig. 6 | The involvement of haem pocket in EasC$_{Cf}$ reaction. **a**, Structural analysis of the haem pocket of EasC$_{Cf}$. The amino residues mutated in this study are shown in line. Residue L39 is from the homodimeric counterpart. Red dashed line indicates distance <3.5 Å. **b**, Protein color of wild-type and variant EasC$_{Cf}$. The concentrations of all proteins are 11.5 mg ml^{-1}. **c**, Mutational studies of the amino residues constructing the haem pocket. The enzyme activity of each sample is calculated as a percentage of the wild type enzyme (WT). The individual (n = 3) and average values along with error bars (s.d.) of each group in one representative experiment among three independent experiments are shown. **d**, CD spectra of conserved amino acid mutants of EasC$_{Cf}$. The blue curve represents CD spectra of the WT, and the red curve represents CD spectra of each mutant. **e**, The detailed inhibitory data of catalase inhibitors (i) NaN_3 and (ii) NH_2OH on EasC$_{Cf}$ catalyzed reaction. Inhibition potency (IC$_{50}$, constant reflecting 50% inhibition) were calculated by a four-parameter logistic equation using GraphPad Prism, v6.0 (GraphPad Software Inc., San Diego, CA). Per cent inhibtion = (Substrate residual rate with inhibitors − Substrate residual rate without inhibitors) × 100%. **f**, Restoration of the activity of NaN_3-inhibited EasC$_{Cf}$ by buffer exchange. The reaction system generally consists of 20 μM EasC$_{Cf}$ enzyme, 0.5 mM **PCC**, 2 mM NADPH, and 100 mM NaN_3. The enzyme activity was measured by the remaining amount of the substrate.

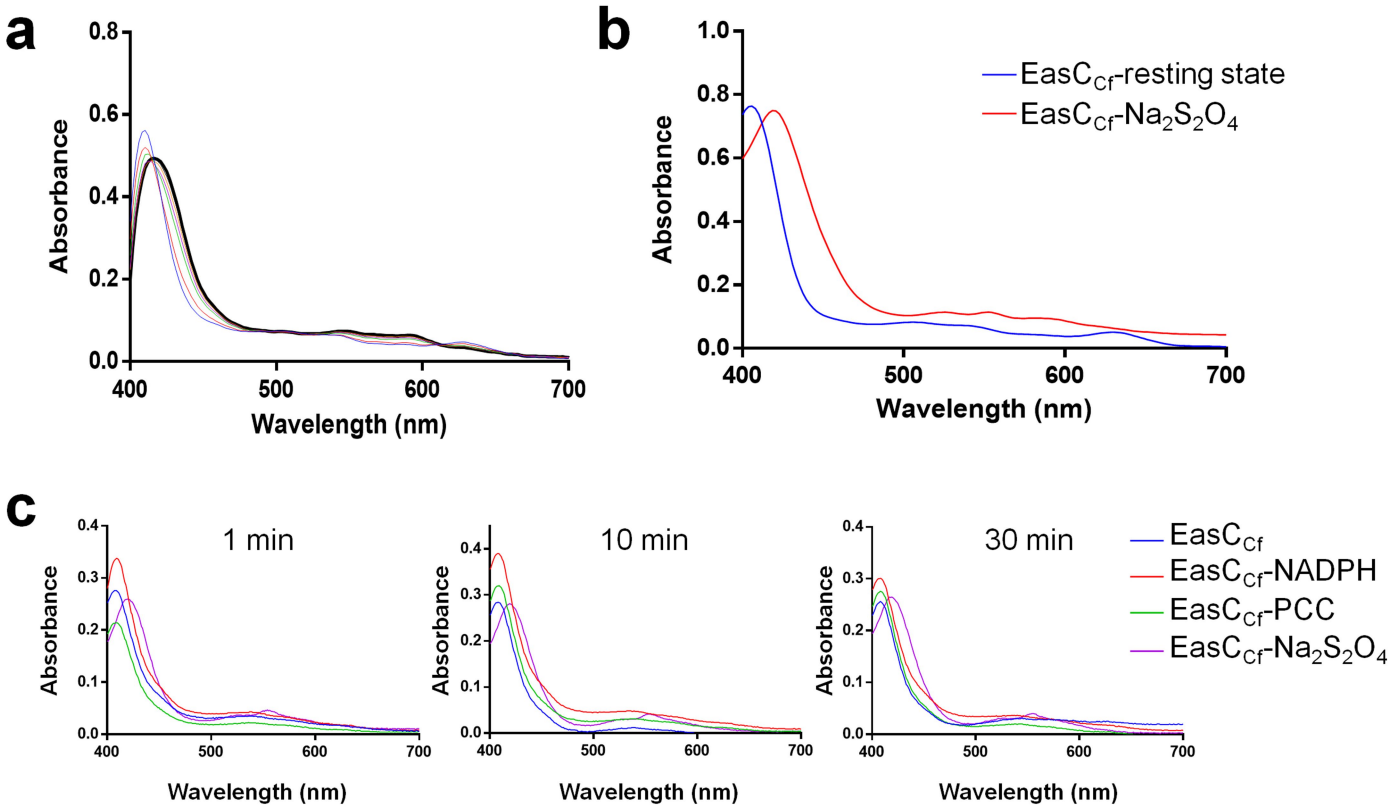

Extended Data Fig. 7 | Probing the reduction conditions of ferric EasC. **a**, The overall view of stopped flow UV-visible spectra obtained on reaction of ferric 40 μM EasC$_{Cf}$ with 0.5 mM **PCC** monitored over 1 s (1, 31, 151, 301, 451, 601, 751 ms). Black line represents the formation of **Cpd III** (λ_{max} = 416, 544, 590 nm). **b**, The overall view of the UV-Vis absorption spectra of EasC$_{Cf}$ protein in resting state and reduced state were tested under anaerobic condition. The reduced protein was produced through adding sodium dithionite with a final concentration of 2 mM. **c**, The UV-Vis absorption spectra of EasC$_{Cf}$ protein under anaerobic condition. A 50 μL typical assay solution contained 50 mM PBS buffer (pH 7.5) and 40 μM enzymes. EasC$_{Cf}$ was incubated with 2 mM NADPH, 2 mM **PCC**, and 2 mM sodium dithionite, respectively.

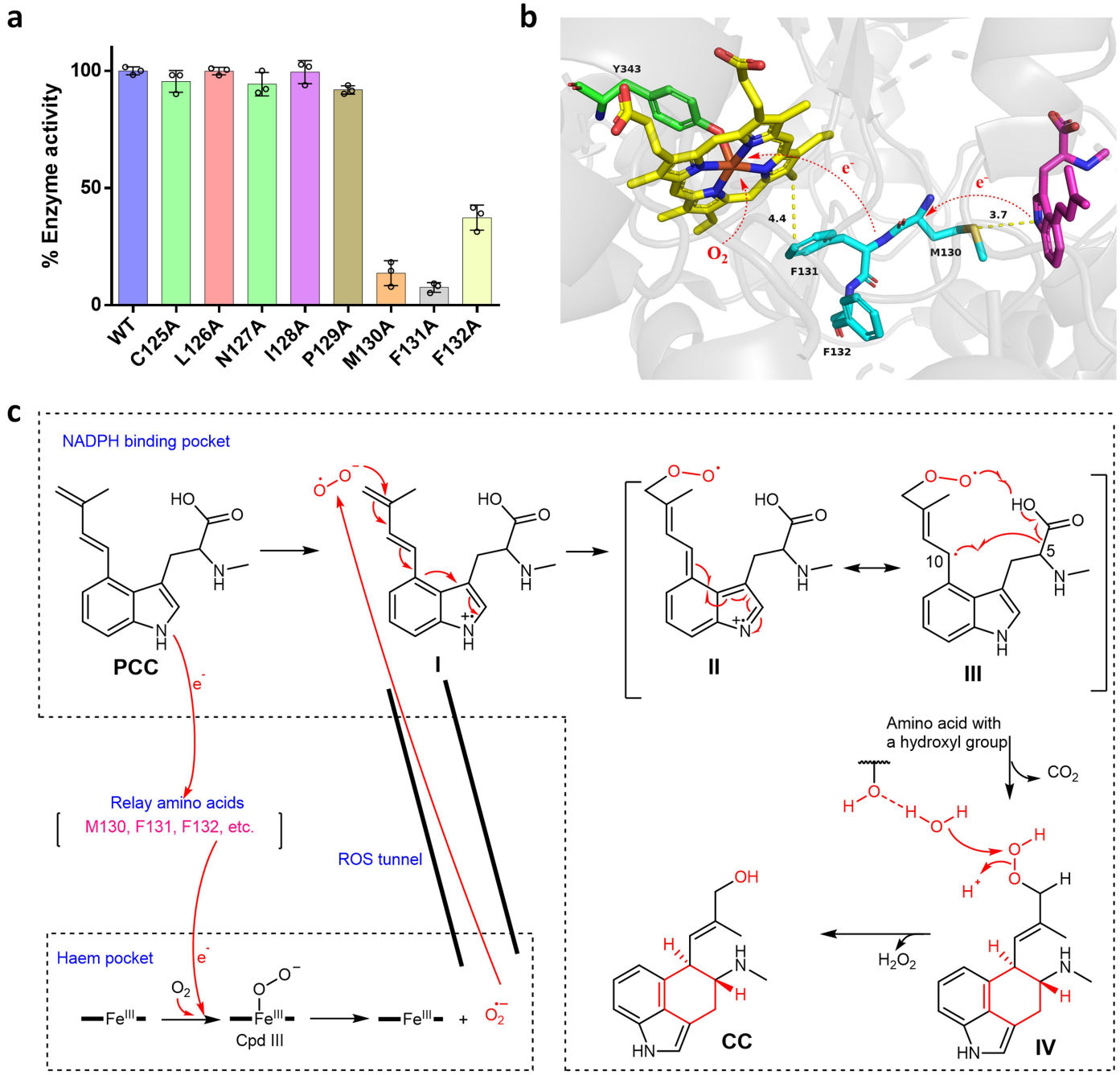

Extended Data Fig. 8 | Proposed mechanism for EasC reaction. a, Mutational results towards the amino acids possibly involving in transferring electron between the haem pocket and the NADPH-binding pocket. The enzyme activity of each sample is calculated as a percentage of the wild type enzyme (WT). The individual ($n = 3$) and average values along with error bars (s.d.) of each group in one representative experiment among three independent experiments are shown. **b**, The proposed long-range electron transfer pathway for $EasC_{Cf}$. The Met-Phe-Phe was proposed to be the group of relay amino acids in the process of binding and activation of O_2. The distance from those three amino acids to **PCC** and haem is measured in Å (angstroms). **c**, Superoxide mediated cooperative catalysis of two pockets in EasC reaction. Upon the binding of O_2, **PCC** in the NADPH-binding pocket donates an electron to Fe(III) in the haem pocket via the relay amino acids M130, F131, and F132 to generate **Cpd III** and the intermediate **I** with a radical cation. **I** was further catalyzed by the superoxide, from the dissociation of **CpdIII**, to generate **II**, featuring a hydroperoxide radical. **II** could equilibrate to the intermediate **III** with a radical at C10. The hydroperoxide radical in **III** could mediate the hydrogen abstraction of the carboxylic acid group to initiate the decarboxylation and the following ring cyclization by radical coupling between C5 and C10 to generate **IV** with a terminal hydroperoxide. The following elimination of H_2O_2 leads to the formation of **CC**, aided by hydrogen bond interactions between the hydroperoxide group and surrounding amino acid residues.

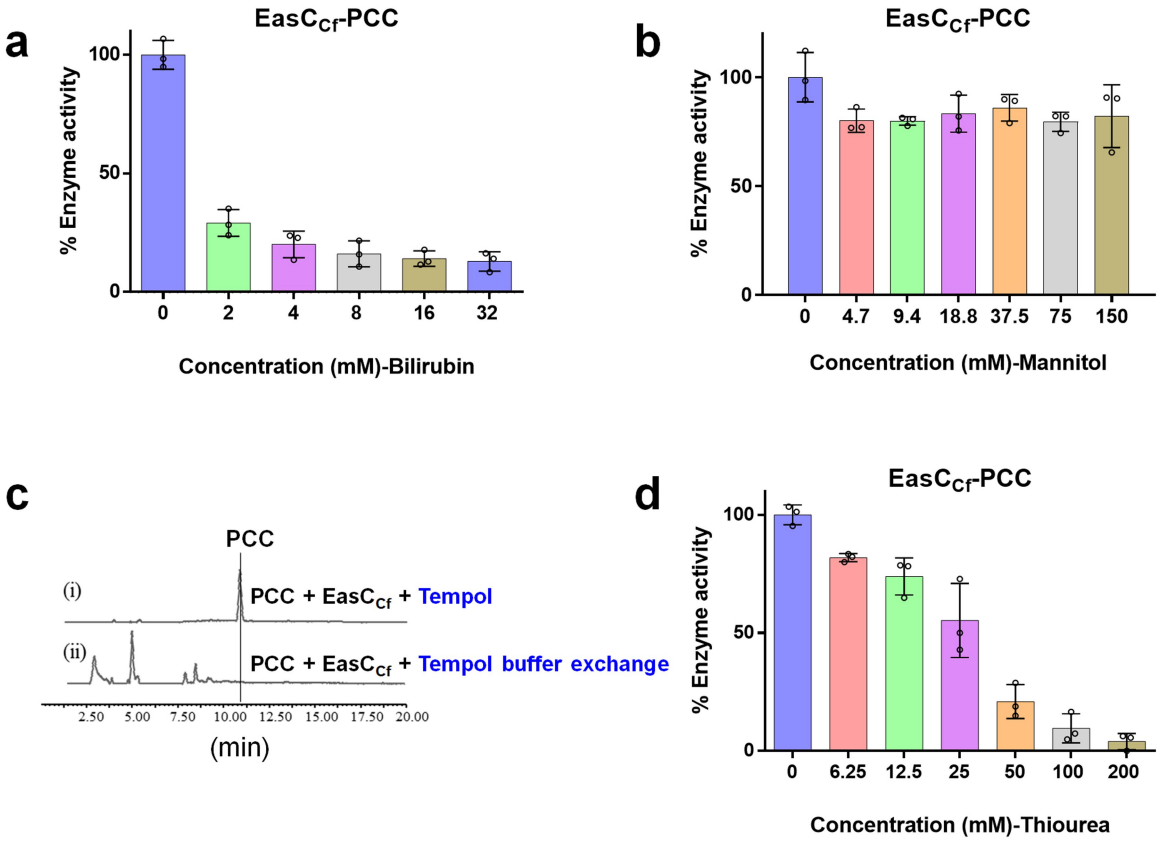

Extended Data Fig. 9 | The effects of ROS scavengers on the EasC$_{cf}$ reaction. **a**, **b**, and **d**, The inhibitory data of ROS scavenger bilirubin, hydroxyl radical (HO•) scavenger mannitol and superoxide scavenger thiourea towards EasC activity. The enzyme activity of each sample is calculated as a percentage of the control sample. The individual (n = 3) and average values along with error bars (s.d.) of each group in one representative experiment among three independent experiments are shown. **c**, Restoration of the activity of tempol-inhibited EasC by buffer exchange. The reaction system is generally consisted of 20 μM EasC enzyme, 0.5 mM **PCC**, 2 mM NADPH, with different concentrations of ROS scavengers, respectively. The enzyme activity was measured by the remaining amount of the substrate.

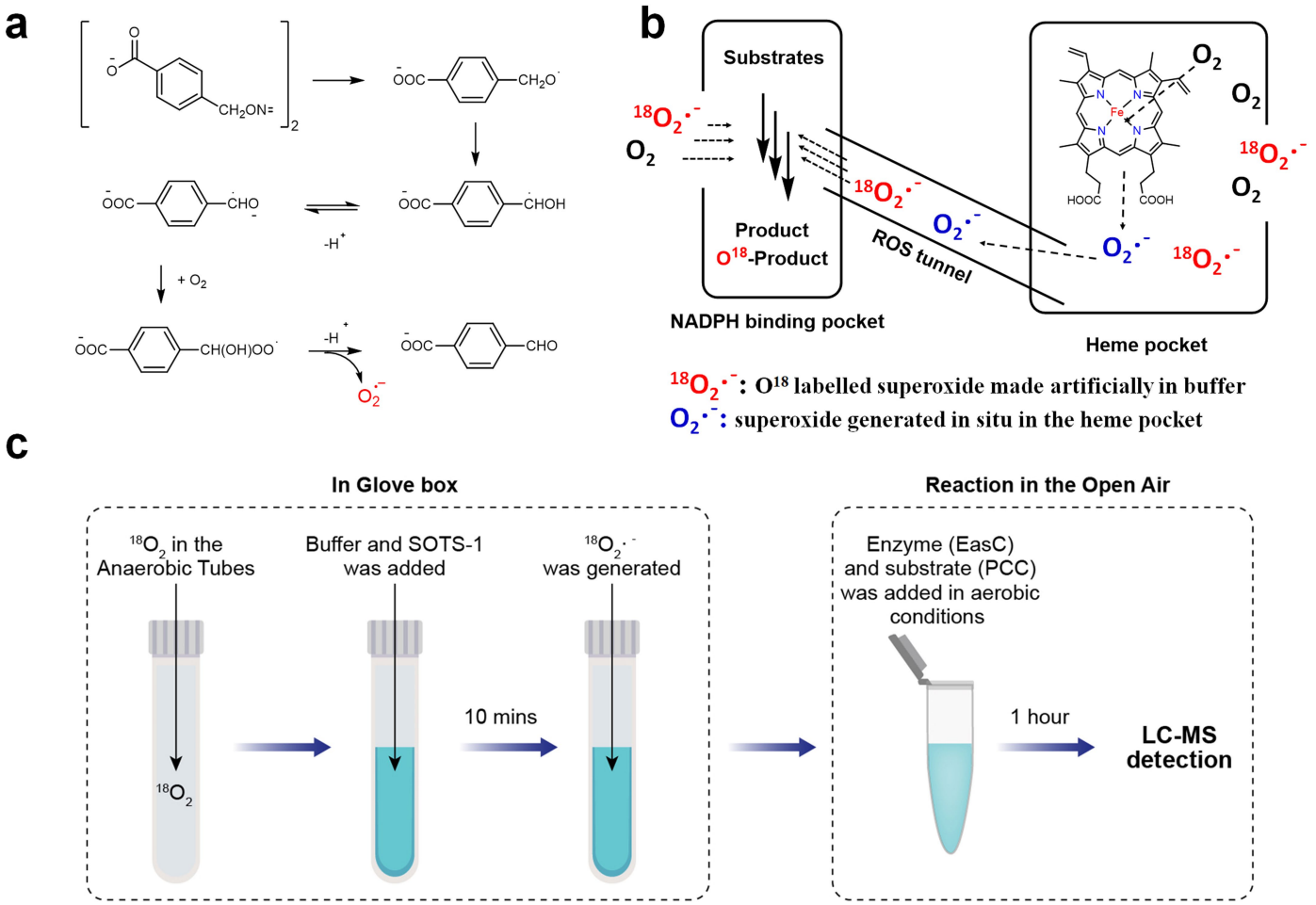

Extended Data Fig. 10 | The competitive incorporation experiment using ^{18}O-superoxide. a, The pathway for SOTS-1 decomposition and its ensuing reaction with oxygen, leading to the release of superoxide. **b**, The illustration of the competitive incorporation experiment using ^{18}O-superoxide in EasC$_{Cf}$ reaction. **c**, The protocol for the artificial production of ^{18}O-superoxide. ^{18}O-superoxide was generated in the glove box by mixing the $^{18}O_2$ with SOTS-1 in the reaction buffer. The buffer with ^{18}O-superoxide was further moved to the open air to get rid of the $^{18}O_2$. The control group follows the same protocol, except that SOTS-1 is not added. EasC noted in the figure is EasC$_{Cf}$.

nature portfolio

Corresponding author(s): Rey-Ting Guo

Last updated by author(s): Dec 23, 2024

Reporting Summary

Nature Portfolio wishes to improve the reproducibility of the work that we publish. This form provides structure for consistency and transparency in reporting. For further information on Nature Portfolio policies, see our Editorial Policies and the Editorial Policy Checklist.

Statistics

For all statistical analyses, confirm that the following items are present in the figure legend, table legend, main text, or Methods section.

n/a	Confirmed	
☐	☒	The exact sample size (*n*) for each experimental group/condition, given as a discrete number and unit of measurement
☐	☒	A statement on whether measurements were taken from distinct samples or whether the same sample was measured repeatedly
☒	☐	The statistical test(s) used AND whether they are one- or two-sided *Only common tests should be described solely by name; describe more complex techniques in the Methods section.*
☒	☐	A description of all covariates tested
☒	☐	A description of any assumptions or corrections, such as tests of normality and adjustment for multiple comparisons
☐	☒	A full description of the statistical parameters including central tendency (e.g. means) or other basic estimates (e.g. regression coefficient) AND variation (e.g. standard deviation) or associated estimates of uncertainty (e.g. confidence intervals)
☒	☐	For null hypothesis testing, the test statistic (e.g. *F*, *t*, *r*) with confidence intervals, effect sizes, degrees of freedom and *P* value noted *Give P values as exact values whenever suitable.*
☒	☐	For Bayesian analysis, information on the choice of priors and Markov chain Monte Carlo settings
☒	☐	For hierarchical and complex designs, identification of the appropriate level for tests and full reporting of outcomes
☒	☐	Estimates of effect sizes (e.g. Cohen's *d*, Pearson's *r*), indicating how they were calculated

Our web collection on statistics for biologists contains articles on many of the points above.

Software and code

Policy information about availability of computer code

Data collection	Data were collected using Waters 2596 Separations Module Empower v3, MicroCal iTC200 Software v1.00, MicroCal PEAQ-ITC, PerkinElmer EnSpire 2300 Multimode Reader Software v4.1, a CORUI (China) HPLC with SPYD infusion pump, SMAA sample injector, UVXB UV-detector, and Software Clarity v7. 4. 1. 88, Waters HPLC-MS with 2596 Separations Module , 2996 Photodiode Array Detector and MassLynx v4.1, Agilent 1260 Agilent Accurate-Mass-Q-TOF MS 6520 with an electrospray ionization (ESI) source and Software MassHunter Workstation vB.04.0, Epoch 2 microporous plate spectrophotometer of Bio Tek Gene5 v3.05, CHUANG HONG Yiqi Anaerobic glove box ZDYY2-III, Stopped-flow apparatus Model SX-20 with Pro-Data SX and Pro-Data Viewer Application version 4.5.1848.0, Circular dichroism spectrometer of Model Chirascan VX and Pro-Data Viewer Application version 4.5.1848.0, Bruker EMXplus spectrometer with a helium-662 flow cryostat, Bruker X-band (9.4 GHz) EMX plus 10/12 spectrometer equipped with an Oxford-910 cryostat and ITC-503 temperature controller (Oxford Instruments Ltd., Oxfordshire, UK), stopped-flow apparatus (Model SX-20) from Applied Photophysics (UK), MicroCal iTC200, Waters HPLC 2596 equipped with a mass spectrum detector (2996), Gaussian 16 C.01 software.
Data analysis	Data were analyzed using Discovery Studio Client 520 v19.1.0, GraphPad Prism, v6.0. HARLEM version 2023-02-20.

For manuscripts utilizing custom algorithms or software that are central to the research but not yet described in published literature, software must be made available to editors and reviewers. We strongly encourage code deposition in a community repository (e.g. GitHub). See the Nature Portfolio guidelines for submitting code & software for further information.

Data

Policy information about availability of data

All manuscripts must include a data availability statement. This statement should provide the following information, where applicable:

- Accession codes, unique identifiers, or web links for publicly available datasets
- A description of any restrictions on data availability
- For clinical datasets or third party data, please ensure that the statement adheres to our policy

All data are available in the main text or the supplementary materials. The 3D cryo-EM density maps of the EasCCf and EasCCf/PCC have been deposited in the Electron Microscopy Data Bank under the accession numbers EMD-61387 and EMD-61388, respectively. The coordinates of the EasCCf and EasCCf/PCC have been deposited in the Protein Data Bank under the accession codes 9JDB and 9JDC, respectively.

Research involving human participants, their data, or biological material

Policy information about studies with human participants or human data. See also policy information about sex, gender (identity/presentation), and sexual orientation and race, ethnicity and racism.

Reporting on sex and gender	n/a
Reporting on race, ethnicity, or other socially relevant groupings	n/a
Population characteristics	n/a
Recruitment	n/a
Ethics oversight	n/a

Note that full information on the approval of the study protocol must also be provided in the manuscript.

Field-specific reporting

Please select the one below that is the best fit for your research. If you are not sure, read the appropriate sections before making your selection.

☒ Life sciences ☐ Behavioural & social sciences ☐ Ecological, evolutionary & environmental sciences

For a reference copy of the document with all sections, see nature.com/documents/nr-reporting-summary-flat.pdf

Life sciences study design

All studies must disclose on these points even when the disclosure is negative.

Sample size	No statistical methods were used predetermine sample size. Three independent experiments with sample size n= 3 were performed.
Data exclusions	No data were excluded from analyses.
Replication	All experiments were performed at least two or three times. All attempts of replication were successful.
Randomization	Randomization was not appropriate to the experiments performed, because no statistical comparisons were performed.
Blinding	Blinding was not relevant, because no statistical comparisons were performed.

Reporting for specific materials, systems and methods

We require information from authors about some types of materials, experimental systems and methods used in many studies. Here, indicate whether each material, system or method listed is relevant to your study. If you are not sure if a list item applies to your research, read the appropriate section before selecting a response.

Materials & experimental systems

n/a	Involved in the study
☒	☐ Antibodies
☒	☐ Eukaryotic cell lines
☒	☐ Palaeontology and archaeology
☒	☐ Animals and other organisms
☒	☐ Clinical data
☒	☐ Dual use research of concern
☒	☐ Plants

Methods

n/a	Involved in the study
☒	☐ ChIP-seq
☒	☐ Flow cytometry
☒	☐ MRI-based neuroimaging

Plants

Seed stocks	n/a
Novel plant genotypes	n/a
Authentication	n/a